Phytoplankton can actively diversify their migration strategy in response to turbulent cues

Citation: Sengupta, Anupam et al. "Phytoplankton Can Actively Diversify Their Migration Strategy in Response to Turbulent Cues." Nature 543, 7646 (March 2017): 555–558 © 2017 Nature Publishing Group

As Published: http://dx.doi.org/10.1038/nature21415

Publisher: Nature Publishing Group

Persistent URL: http://hdl.handle.net/1721.1/111154

Version: Original manuscript: author's manuscript prior to formal peer review

A phytoplankton population actively diversifies its migration strategy in response to turbulent cues

Anupam Sengupta[1,2,*], Francesco Carrara[1,2,*] and Roman Stocker[1,2,#]

[1] Institute for Environmental Engineering, Department of Civil, Environmental and Geomatic Engineering, ETH Zurich, 8093 Zurich, Switzerland

[2] Ralph M Parsons Laboratory, Department of Civil and Environmental Engineering, Massachusetts Institute of Technology, Cambridge 02139, Massachusetts, USA

[*] These authors contributed equally to this work

[#] Corresponding author: romanstocker@ethz.ch

Abstract

Marine phytoplankton inhabit a dynamic environment where turbulence, together with nutrient and light availability, shapes species fitness, succession, and selection[1,2]. Many species of phytoplankton are motile and undertake diel vertical migrations to gain access to nutrient-rich deeper layers at night and well-lit surface waters during the day[3,4]. Disruption of this migratory strategy by turbulence is considered to be an important cause of the succession between motile and non-motile species when conditions turn turbulent[1,5,6]. However, this classical view neglects the possibility that motile species may actively respond to turbulent cues, in order to avoid layers of strong turbulence[7]. Here we report that a population of the harmful-algal-bloom forming raphidophyte *Heterosigma akashiwo* actively diversifies its migratory strategy in response to hydrodynamic cues characteristic of overturning by Kolmogorov-scale eddies. Upon experiencing repeated overturning with timescales and statistics representative of ocean turbulence, an upward swimming population rapidly (5–60 min) splits into two subpopulations, one swimming upward and one swimming downward. Quantitative morphological analysis together with a model of cell mechanics revealed that this behaviour was accompanied by a modulation of the cells' fore-aft asymmetry. The minute magnitude of the required modulation, sufficient to invert the cells' preferential swimming direction, highlights the advanced level of control that phytoplankton can exert on their migratory behaviour. Together with observations of enhanced cellular stress following overturning and the typically deleterious effects of strong turbulence on motile phytoplankton[5,8], these results point to an active adaptation of *H. akashiwo* to increase the chance of evading turbulent layers by diversifying the direction of migration within the population, in a manner suggestive of evolutionary bet-hedging. This migratory behaviour, which we observed also in other raphidophyte and dinoflagellate strains, relaxes the boundaries between the fluid dynamic niches of motile and non-motile phytoplankton, and highlights that rapid responses to hydrodynamic cues are important survival strategies for phytoplankton in the ocean.

Understanding the distribution of phytoplankton in the ocean represents a longstanding challenge in oceanography[9], owing to the complex, multi-scale interactions between biotic and abiotic processes[10]. Unfavourable conditions, such as light and nutrient limitation[2], sub-optimal temperature[11] or strong turbulence[5] can cause physiological stress and reduced growth, affecting species fitness and succession[1,2,12]. Phytoplankton have evolved diverse adaptive strategies to cope with environmental stressors, often by exhibiting plasticity in important functional traits[13], including buoyancy[14], chlorophyll[13] and lipid content, which they can modulate in response to ambient conditions.

Turbulence is a prevalent physical factor in the ecology of phytoplankton, and is implicated in the seasonal succession and bloom formation of phytoplankton species[1,2,9], as first conceptualized in Margalef's 'mandala'[1,12]. Turbulence is often deleterious for the physiology of motile phytoplankton[5,6], causing flagellar or body wall damage, reduced lipid production and impaired organelle functioning[8]. Because turbulence is often intermittent and localized[7], frequently affecting only a few meters of the water column[15], migration could be an effective turbulence-avoidance strategy. However, this hypothesis implies that phytoplankton can modulate migration based on turbulent cues, which has not been demonstrated until now.

Evidence for behavioural responses of phytoplankton to turbulence has remained scarce and limited primarily to drag reduction over timescales comparable to the cell cycle[16]. Here we demonstrate an active, rapid and fine-tuned response of a phytoplankton species to a fundamental turbulent cue. We show that the raphidophyte *Heterosigma akashiwo* – known for its allelopathic effects[17] and toxic blooms, and frequently used as a model system for vertical migration studies[4,18] – diversifies its migration behaviour upon repeated overturning events that mimic the effect of small-scale eddies, with nearly half of an upward-swimming population engaging in a dive response within 30 minutes. Because the vertical is the most effective direction for modulating migration in order to escape unfavourable conditions, we propose that this rapid behavioural diversification may be a bet-hedging strategy to increase chances of evading turbulent layers.

Many phytoplankton species rely on gravitaxis[19] to migrate through the water column. Gravitaxis is a form of directed motility mediated by a stabilizing torque that biases swimming in the vertical direction. In the presence of hydrodynamic shear, gravitactic swimming can lead to the formation of thin layers[18], while in turbulence it can cause microscale patchiness in cell distribution[20]. These phenomena represent passive effects of flow on swimming cells: whether cells can actively modulate gravitaxis and thus their direction of migration in response to turbulence has remained unknown.

We observed and tracked individual cells of *H. akashiwo* (strain CCMP452, hereafter referred to as HA452) in a millifluidic chamber ($4\times12\times1.6$ mm^3) using video microscopy. The chamber could be continuously rotated around a horizontal axis by means of a computer-controlled motor, thus mimicking the overturning of cells in the ocean by Kolmogorov-scale

eddies (Fig. 1a,b). In the absence of rotation, cells exhibited a strong tendency to swim upwards (negative gravitaxis), resulting in a marked accumulation at the top of the chamber (Fig. 1c).

Repeated overturning caused a striking departure from negative gravitaxis. We first imposed a periodic series of flips, with a period (18 s) representative of the Kolmogorov timescale in the ocean (0.1–30 s) ([7]), the characteristic overturning time of the smallest eddies. Specifically, a period of 18 s corresponds to a turbulent dissipation rate $\varepsilon = 3\times10^{-8}$ W/kg, characteristic of the ocean's pycnocline[21]. When exposed to this overturning regime for 30 min (100 flips), the population split into two subpopulations: HA452(↑) continuing to swim upwards (negative gravitaxis) and accumulating at the top of the chamber, HA452(↓) swimming downwards (positive gravitaxis) and accumulating at the bottom (Fig. 1d). The population split occurred both for populations cultured under continuous light and for populations cultured under a diel light cycle (Materials and Methods). We quantified the population split in terms of an upward bias index, $r = (f_{\uparrow} - f_{\downarrow}) / (f_{\uparrow} + f_{\downarrow})$, with $f_{\uparrow}$ and $f_{\downarrow}$ the concentrations of cells in the top and bottom 400 µm of the chamber, respectively (Fig. 1g). The treatment with 100 flips resulted in $r = 0.13\pm0.20$, whereas control experiments with cells held in the chamber for 30 min without flipping yielded no population split ($r = 0.61\pm0.12$; Fig. 1g). A starved HA452 population exhibited no split (Extended Data Fig. 1d), suggesting that behavioural responses to turbulence depend on the cells' physiological state. Sinking was ruled out as the cause of the bottom accumulation, because cells from both subpopulations exhibited active swimming with comparable speed (top: 74.5±42.4 µm s^{-1}; bottom: 73.8±46.2 µm s^{-1}; Extended Data Fig. 2), indicating that the split is an active behavioural adaptation to overturning.

The population split occurred also for reorientations that were not purely periodic, and were instead directly modelled on the continuous, stochastic reorientation experienced by cells in isotropic turbulence, obtained from a Direct Numerical Simulation (Fig. 1b; Methods). After 30 min, the continuous reorientation treatment resulted in $r = 0.22\pm0.04$, denoting a population split of the same magnitude as the periodic flipping case (ANOVA: $p < 0.001$, Extended Data Table 1; Fig. 1g). This finding justifies the simplification of using flips in lieu of continuous, stochastic reorientations. While the hydrodynamic environment in the flip chamber is not equivalent to turbulence, it captures the overturning of cells by small-scale turbulent eddies, also in terms of timescales.

The magnitude of the population split increased with the duration of the overturning treatment (Fig. 2a). Over the course of 30 flips (~10 min) the upward bias r decreased from 0.61 to 0.30, corresponding to a 60% increase in the number of down-swimming cells. This fast change indicates that the response is rapid and even brief periods of turbulence can cause diversified migration. The response saturated after 300 flips (~2 h) at $r = 0.03\pm0.10$, which corresponds to a symmetrical distribution of up- and down-swimmers.

The migratory response was triggered by changes in the cell orientation relative to gravity. This was revealed by additional periodic flipping experiments, with the same periodicity but in the horizontal plane (Fig. 1g). No population split was observed in this case (r = 0.48±0.16 after 30 min; Extended Data Table 1). The change in cell orientation relative to gravity is a simple yet fundamental effect of a small-scale turbulent eddy on plankton. Compared to it, the hydrodynamic acceleration of the fluid in an eddy (~0.001g) ([22]) is negligible, indicating that a reversal of the perceived gravitational acceleration, rather than fluid velocity gradients, represents the cue for the behavioural differentiation (Supplementary Information).

The switch of a fraction of the cells to downward swimming corresponded to a switch in their orientational stability. The latter is quantified by the reorientation timescale, B, the characteristic time a cell takes to rotate back to its vertical equilibrium orientation once perturbed from it. A greater magnitude of B denotes less stability and the sign of B denotes upward ($B > 0$) or downward ($B < 0$) stability (Methods). For the up-swimming cells we found B = 10.4±1.5 s prior to flipping (Fig. 2b). After 30 min of flipping, two behaviourally distinct subpopulations of HA452 cells emerged. Cells from these two subpopulations, HA452(↑) and HA452(↓), had lost stability and, most importantly, had opposite stability, with $B_{\uparrow}$ = 19.3±13.5 s and $B_{\downarrow}$ = -23.1±10.2 s (Fig. 2c), confirming the active nature of the down-swimming behaviour.

The process underpinning the reversal in stability responsible for the emergence of down-swimming cells was a change of morphology. We harvested cells from the top and bottom of the chamber after 30 min of flipping and determined their shape through phase contrast microscopy. We found that up-swimming cells were fore-aft asymmetric, narrower in the front and wider in the back (Fig. 1e, Extended Data Fig. 3). In contrast, down-swimming cells were fore-aft symmetric (Fig. 1f). Quantitative image analysis showed that the asymmetry was on the order of 1 μm – a minute yet robust morphological difference between the two subpopulations (Extended Data Fig. 3 and Table 2; Methods). This fast shape change is enabled by the absence of a rigid cell wall, characteristic of many raphidophytes[23], conferring HA452 cells considerable morphological plasticity.

A cell mechanics model demonstrated that the observed shape change is sufficient to cause the stability switch. Using the cell contour, the size and position of the nucleus determined by epifluorescence microscopy, and the flow field around the cell obtained through a computational fluid dynamics model (Methods), we determined the position of the three points relevant for cell stability: the geometric centre, C_B (where the buoyancy force acts), the centre of mass, C_W (where the weight acts), and the centre of hydrodynamic stress, C_H (where the resultant hydrodynamic force acts) (Fig. 3, Extended Data Fig. 3, Tables 2 and 3) (Methods). For HA452 cells collected from the top of the chamber after 30 min of flipping (subpopulation HA452(↑)), we found that C_W was located a distance L_W = 0.03±0.04 μm above C_B (Fig. 3a,b), making cells top-heavy. By itself, this top-heaviness produces a torque T_W that orients cells downwards. However, because of the fore-aft asymmetry, C_H was located a distance L_H = 1.17±0.46 μm above C_B (Fig. 3b; Extended Data Figs. 3,4),

producing a torque $T_H > T_W$ that overcame top-heaviness and oriented cells upwards. In contrast, for cells collected from the bottom of the chamber after 30 min of flipping (subpopulation HA452(↓)), L_W was unchanged (0.04±0.04 µm), but L_H was reduced (0.24±0.27 µm; Fig. 3c,d Extended Data Figs. 3,4), because of the loss of front-aft asymmetry. As a result, $T_W > T_H$ and cells were stable downwards (Fig. 3d). In the phase space of cell stability defined by the two cellular length scales L_H and L_W the loss of fore-aft asymmetry corresponds to the crossing of the line dividing upward from downward stability regimes (Extended Data Fig. 5).

For comparison, for a different strain of *H. akashiwo* (HA3107) that had greater, upward stability (B = 4.9±1.5 s; Extended Data Fig. 6), we found that C_W was located a distance L_W = 0.02±0.02 µm below C_B (bottom-heavy; Fig. 3e,f) and C_H was located a distance L_H = 0.87±0.23 µm above C_B (Fig. 3f; Extended Data Figs. 3,4), so that both torques T_W and T_H stabilized cells upwards. Indeed, HA3107 did not exhibit a behavioural split, but the entire population retained upward stability upon repeated flipping (Fig. 2a).

These observations reveal that HA452 is capable of rapid polymorphism to diversify its migration strategy. Polymorphism is an important adaptation in phytoplankton[24], yet to date has been observed mostly as large morphological changes occurring over demographic timescales, for example in the reversible loss of horns and spines to accelerate sinking[16] or in chain formation[5]. In contrast, HA452 diversifies shape over minutes, and a minute morphological change is sufficient to drastically alter migration behaviour. These findings thus illustrate exquisite control over movement behaviour through fine-scale control over cellular morphology.

The mechanism by which HA452 perceives its reorientation relative to gravity remains unclear. The large (>75 µm) unicellular protists *Paramecium* and *Tetrahymena* directly sense gravity through mechanosensitive ion-channels, which are activated by the gravitational pressure of the cytoplasm on the lower membrane[25]. However, in the size range of HA452 (~15 µm) the work from gravitational pressure is comparable to thermal noise (10^{-21} J; Supplementary Information), making this mechanism unlikely. On the other hand, cross-talk between ion-channels and reactive nitrogen species (RNS) production has been observed[26], suggesting that the sensing of gravity may involve positive feedbacks between these two cellular networks.

We propose that the observed diversification of migration strategies is an escape response to avoid turbulence. The behaviour we reported could afford significant benefits to a migrating population when turbulence is heterogeneous over the depth of the water column, as often occurs in the ocean where turbulent layers or patches often span no more than a few meters in depth[7,15]. When an upward migrating phytoplankton population enters a turbulent layer, part of the population may switch to downward migration (temporarily renouncing to performing photosynthesis and thus to growing) in response to the turbulent reorientations and thus avoid exposure to the stronger and potentially damaging levels of turbulence in the

core of the layer. Damages from strong turbulence to motile phytoplankton have been extensively reported and include disruptions to diverse elements of their complex life cycles, including the cellular clock, mitotic cycle, nucleic acid concentration, disturbance of microtubule assembly and chromosome separation, reduction in swimming velocity and loss of flagella[5,8]. At the same time, uncertainty about the severity of turbulence in any particular layer implies that a strategy of splitting allows some cells to attempt the 'crossing' of the layer, with the benefit of continued growth at the risk of turbulent damage.

This population split may be a bet-hedging strategy (sensu Bulmer[27]) to cope with the encounter of a turbulent layer in the ocean during vertical migration. According to this scenario, by phenotypically diversifying into two subpopulations with different gravitactic behaviours, a population increases the probability that at least a fraction of the cells escape turbulence, at the cost of reduced photosynthesis because downward swimming cells will not reach well-lit surface waters (Supplementary Information). This hypothesis is supported by the observation that re-growing cells collected from the bottom of the chamber after the overturning treatment resulted in a recovery of the original upward stability (Extended Data Fig. 1a,b). The occurrence of a split upon flipping also in a monoclonal population of HA452 (Extended Data Fig. 1c) strongly suggests that genetically identical cells can express different gravitactic phenotypes. The high intrinsic variability in the reorientation timescale B within the population – prior to and thus independently of the reorientation treatment – is also in line with the bet-hedging hypothesis (Extended Data Fig. 7, Supporting Information), because it allows a diversification of migration strategies through inversion of the orientational stability of a fraction of the cells in the population. However, other mechanisms that produce phenotypic differences cannot be ruled out, including ones that produce changes to the DNA sequence, as occurs in genetic switching[28]. Genetic switching may also in principle have occurred in our monoclonal population and would not be straightforward to distinguish from phenotypic heterogeneity[29].

The escape hypothesis finds support in stress measurements, performed by quantifying the production of the free radical nitric oxide (NO) (Methods), which revealed that flipping is stressful for HA452 (Supplementary Information). After flipping, cells from the two subpopulations showed significantly higher rates of NO accumulation ($3.9\pm0.5 \times 10^{-3}$ s^{-1} for HA452(↓); $2.9\pm0.3 \times 10^{-3}$ s^{-1} for HA452(↑); Fig. 4) compared to the still control ($2.1\pm0.3 \times 10^{-3}$ s^{-1}; Kruskal-Wallis test: $p = 0.02$, Extended Data Table 4). By demonstrating that flipping causes stress, these results confirm the view of turbulence being typically deleterious for motile phytoplankton[1,5,8] (although it can be beneficial for some species[6], in particular by enhancing mass transport to larger cells[30]) and supports the hypothesis that a diversification of migration strategies can aid HA452 escape from turbulent regions.

Adaptation phenomena to turbulence in phytoplankton are not restricted to HA452 and could be widespread. Additional experiments revealed that several other raphidophytes and dinoflagellates responded to flipping by modifying their vertical migration pattern, in some cases in a manner very similar to that of HA452 (Extended Data Fig. 8 and Table 5).

Margalef's mandala has remained the paradigm for the effect of turbulence on phytoplankton species succession in the ocean[1,2,12]. The results reported here suggest that active responses of cells to turbulence may play an important role in this paradigm, and that the spatial structure of turbulence – not just its intensity – may be a fundamental driver of phytoplankton species fitness and succession[2]. We thus propose that the understanding of the ocean embodied in the mandala should be augmented by a mechanistic understanding of behavioural adaptations to turbulence, to better understand how turbulence shapes phytoplankton community composition in present-day and future environmental conditions.

Materials and Methods

Cell culture. Two different strains of the raphidophyte *Heterosigma akashiwo* were examined: CCMP 452 (obtained from the National Center for Marine Algae; here referred to as 'HA452') and CCMP 3107 ([31]) (courtesy of Susanne Menden-Deuer, University of Rhode Island; here referred to as 'HA3107'). Both strains were grown in 50 mL sterile glass tubes at 21°C under continuous illumination (75 μmol m^{-2} s^{-1}), in f/2 (minus silica) media. For propagation, multiple cultures, separated by a few days, were inoculated, and every two weeks 25 mL of fresh media were inoculated with 2 mL of the old culture. Additional experiments were performed (i) with cells grown under a diel light cycle (14 h light / 10 h dark) (Extended Data Fig. 1) and (ii) with monoclonal cultures of HA452. The latter were grown from a single parent cell, isolated from a prior culture by means of an inoculation loop (diameter ~100 μm) developed in house. The loop was dipped into a culture to trap a thin liquid layer and microscopy analysis was used to select the cases with only a single HA452 in the layer. Each single trapped cell was then transferred to a separate well in a 36-well plate containing fresh growth media. Monoclonal cultures were also grown under a 14/10 light cycle (Extended Data Fig. 1c). Experiments were conducted at room temperature (21°C), between 96 h and 120 h after inoculation. This time window corresponds to the early exponential growth phase of HA452 (Extended Data Fig. 9a). All experiments were carried out at a specific time of the day (9-12 am) to rule out any possible artefact due to the diurnal migration pattern of *H. akashiwo* (Extended Data Fig. 9b).

Flipping chamber. All experiments were conducted in a millifluidic chamber (12 mm × 4 mm × 1.6 mm) constructed out of a transparent acrylic sheet and mounted on a supporting frame. The frame was coupled to the shaft of a stepper motor and designed to allow for full rotations from 0° to 360°. The rotation of the chamber was automated using an externally programmed controller that drove the motor, with full user-control over the time series of the rotation angle. A suspension of *H. akashiwo* was gently pipetted into the chamber through one of two injection ports which were then closed with silicone plugs. At the end of an experiment, the two ports were used to harvest cells from the top and bottom parts of the chamber using a microcapillary attached to an aspirator tube for gentle suction, for subsequent microscopic characterization. The dimension of the capillary (internal diameter = 500 μm) was chosen to avoid cell damage during sampling.

During experiments, cells in the flipping chamber were visualized using a stereoscope (Nikon SMZ1000) with a plan APO 1× objective (0.12 NA) and a digital CMOS camera (Photron FastCam SA3). The flipping chamber was mounted on a translation stage, the position of which could be controlled using micrometer screws along all three axes. The camera was focused on a plane perpendicular to the rotation axis and halfway between the two chamber walls. The depth of focus was 750 μm, ensuring that cells were more than 400 μm (>50 cell radii) from the front and back walls of the chamber, to eliminate wall effects. Any small residual wall effects that may still have occurred would have been present for the entire duration of an experiment, and thus could not have caused the population split.

Images were acquired at 60 frames per second. The suspension was uniformly illuminated using a single 627 nm LED (0.1 W) mounted just outside of the flipping chamber. Neither of the two *H. akashiwo* strains tested showed any phototactic bias to wavelengths of light in the red spectrum, in agreement with literature[32]. All experiments were conducted under diffused room light settings, to avoid possible photo-responses.

For each treatment, a control experiment was performed consisting in observing cells in the flipping chamber without rotation, for the same time as the duration of the treatment. The vertical distribution of cells in these control experiments was quantified at regular intervals to ascertain that the cells' upward bias in the absence of overturning remained constant (Fig. 2a, red line; Extended Data Fig. 9b).

Overturning experiments. The range of length scales characteristic of a given turbulent flow is quantified by the Taylor Reynolds number, $\mathrm{Re}_\lambda = u_{\mathrm{RMS}}\,\lambda/\nu$, where $\lambda = u_{\mathrm{RMS}}\,(15\nu/\varepsilon)^{1/2}$ is the Taylor length scale, u_{RMS} is the root-mean-square fluid velocity, and ε is the energy dissipation rate. Periodic flipping consisted of multiple, rapid overturnings of the chamber (180 degrees in 3 s), each followed by 15 s at rest. The resulting period of 18 s corresponds to the Kolmogorov timescale $\tau_\eta = (\nu/\varepsilon)^{1/2}$, associated with a turbulent dissipation rate $\varepsilon = 3\times10^{-8}$ W/kg. This value is typical of the ocean pycnocline[21] and falls within the typical range of values for ocean turbulence[7] (10^{-9} – 10^{-5} W/kg).

To drive the timeseries of the angular orientation of the flipping chamber relative to the vertical in the continuous, non-periodic overturning experiments, we used the time history of the angular orientation of a small passive sphere in homogeneous isotropic turbulence, quantified from a direct numerical simulation (DNS) ([20]) at $\mathrm{Re}_\lambda = 65$ (time history courtesy of Massimo Cencini and Guido Boffetta).

Vertical cell distribution. Histograms of normalized cell concentration in the vertical direction inside the flipping chamber, within the region captured by the camera (4 mm × 4 mm), were obtained by identifying the positions of the centroids of individual cells, imaged in the mid-chamber plane (*i.e.*, equidistant from the two sidewalls perpendicular to the

imaging axis). After the end of every flipping experiment, we allowed the population to reach their equilibrium distribution over the vertical by waiting 30 min. This waiting time was chosen conservatively based on the observation that the concentration profile stabilizes already after ~5 min (Extended Data Fig. 10), and the consideration that cells swimming upward at ~50 μm/s (Extended Data Fig. 2) cover the depth of the flipping chamber (4 mm) in < 2 min.

Upward bias index. To quantify the asymmetry in cell distribution over the vertical, we computed the upward bias $r = (f_\uparrow - f_\downarrow) / (f_\uparrow + f_\downarrow)$, where $f_\uparrow$ and $f_\downarrow$ are the numbers of cells in the top 400 μm (↑) and the bottom 400 μm (↓) of the chamber, respectively. A symmetric distribution of cells corresponds to $r = 0$, whereas preferential upward-swimming corresponds to $r > 0$ and preferential downward-swimming to $r < 0$. The two subpopulations HA452(↑) and HA452(↓) were composed of HA452 cells collected from the top/bottom of the chamber after 30 min of flipping.

Cell tracking. For tracking, cell locations were determined by image analysis based on intensity thresholding using MATLAB (The MathWorks) routines. Cell trajectories, obtained from movies recorded at 60 frames per second, were assembled by linking locations of cells in subsequent frames, based on proximity and kinematic predictions from previous time steps, using automated software[33].

Quantification of cell stability. To determine cell stability, we quantified the rotation rate ω of cells as a function of their orientation θ relative to the vertical. This is an established method[19] for quantifying the reorientation timescale B, and is based on the fact that greater stability will cause faster reorientation towards the stable orientation after a cell is perturbed from it. To this end, we tracked individual cells over 15 s immediately following a single flip (which provided the perturbation from the stable orientation), and averaged their rotation rate over all cells as a function of θ. Given that the smallest dimension of the field of view is along the optical axis (750 μm, the depth of field) and that cells swam on average at 70 μm/s, an estimated residence time in the field of view is ~10 s. Tracked trajectories in our dataset are as long as 22 s, with an average of 5.5 s, which is sufficient to compute the stability parameter B. The resulting data for $\omega(\theta)$ were well fitted with a sinusoidal function of the form $A\cos(\theta+\kappa)$, where we imposed a phase shift κ equal to $-\pi/2$ for the top population and $\pi/2$ for the bottom population. (Simultaneously fitting both A and κ showed consistent results to this approach). We determined the reorientation timescale from the best-fit sinusoid as[19] $B = (2A)^{-1}\cos(\pi/2+\kappa)$. To account for heterogeneity in the population stability (Supplementary Information), resulting in some cells reorienting faster than others, we separately quantified B for the first 5 s and the subsequent 10 s (Extended Data Fig. 7a). HA452 cells in the flipping chamber swam in helical patterns, characteristic of many phytoplankton species[34]. However, the helical component was averaged out using a 1-s moving average to reduce noise in the calculation of the stability parameter B.

Axial symmetry, fore-aft asymmetry, and centre of buoyancy. To determine the morphology of cells sampled from the millifluidic chamber, we used single-cell imaging with an inverted microscope (Nikon TE2000) equipped with a 20× or 40× objective and an Andor iXon Ultra 897 camera. We used phase contrast microscopy to determine the cell orientation, through the location of the flagellum that is located on the anterior part of the cell, and the cell contour. To assess the axial symmetry of the cell shape, we acquired images of the cross-section of ten randomly chosen HA452 cells. This was achieved by acquiring videos of each cells over tens of seconds, manually refocusing as needed to maintain cells in focus. From each video, we identified the frames in which cells swam vertically – changing swimming plane – based on the fact that the cell boundary is in sharp focus when a cell swims vertically out of the imaging plane, but is blurry due to optical diffraction when it swims out of the imaging plane at an angle. The frame of the video in which the cell had the maximum diameter was then chosen to extract the cell's cross-section ('top view', Extended Data Fig. 3d). Using this data, we quantified the ratio (R) between the major (b_x) and minor (b_y) semi-axes of the ellipse that best fitted the top-view cross-section (Extended Data Fig. 3). This yielded $R = b_x / b_y = 1.08 \pm 0.06$ (average ± s.d.), *i.e.*, an aspect ratio very close to that of a circle ($R = 1$). Given the small departure of R from 1, the analysis was conducted assuming axial symmetry, with $b = b_x = b_y$. The cell shape was captured by the 3-parameter surface[35]

$$ab / (a^2 \cos^2\gamma \cos^2\delta + a^2 \cos^2\gamma \sin^2\delta + b^2 \sin^2\gamma)^{1/2} + c \sin\gamma = r(\gamma,\delta)\,, \qquad (1)$$

where γ and δ are the polar and azimuthal angles measured from the major axis, a and b are the major and minor semi-axes of an original axisymmetric ellipsoid (i.e., a spheroid), respectively, c measures the deviation from the symmetric shape in the fore-aft direction (*i.e.*, along the major axis), and $r(\gamma,\delta)$ is the distance of a point on the surface from the origin with a polar angle γ and azimuthal angle δ. To quantify a cell's fore-aft asymmetry, the cell contour obtained from phase contrast microscopy was fitted with the curve $ab / (a^2 \cos^2\gamma + b^2 \sin^2\gamma)^{1/2} + c \sin\gamma = r(\gamma,\delta=0)$. The contours of 10 HA452 cells collected from the bottom of the flipping chamber, 13 HA452 cells collected from the top, and 12 HA3107 cells collected from the top (all after 30 min of flipping treatment) were determined through image analysis and used to determine the parameters a,b and c for each population (Extended Data Figs. 3,4). The centre of buoyancy of the cell C_B, which is the center of mass of the (uniform) fluid displaced by the cell, was then determined by finding the geometric centre of the fitted contours.

Centre of mass. To locate a cell's centre of mass, C_W, one needs – in addition to the cell contour – the location, size and density of any heavy organelle. Of particular importance is the nucleus, because of its size and density, and we used epifluorescence microscopy to identify its size and location. The chloroplasts, having higher density than the rest of the cell, could also potentially have contributed to the location of the centre of mass, but in HA452 and HA3107 they are randomly distributed, close to the external membrane, and our analysis showed that their contribution to the offset of the centre of mass, is negligible compared to the contribution of the nucleus. Chlorophyll autofluorescence imaging in HA452 cells

showed that a cell has typically 15–25 chloroplasts, each 1.5 μm in diameter, in agreement with previous observations[23]. In the analysis, we considered 20 chloroplasts per cell, each having a diameter of 1.5 μm and a density ρ_{chlo} = 1150 kg m^{-3} (higher than the density of the rest of the cell, ρ_{cyto} = 1050 kg m^{-3}) ([36]). Chloroplasts were assumed to be distributed randomly on the interior of the cell surface, such that their outmost point was in contact with the cell surface (Extended Data Fig. 4b,c), the location where their contribution to the offset is greatest. The contribution of the chloroplasts to the offset of the center of mass was found to be negligible compared to the contribution of the nucleus (Extended Data Fig. 4c). Prior to imaging, the nucleus was fluorescently stained by incubating cells for 20 min in the dark with 100 nM SYTO 9 (Molecular Probes, Life Technologies), a green fluorescent nucleic acid stain (ex/em 485/498 nm) that stains the nucleus (Extended Data Fig. 3). The intensity of the excitation light was maintained low to prevent photo-toxicity. HA452 and HA3107 cells have the nucleus typically located off-centre. By means of image analysis, we determined the size of the nucleus as well as the distance $L_N = (L_{Na}^2 + L_{Nb}^2)^{1/2}$ between the centre of the nucleus and the centre of buoyancy (Extended Data Fig. 3, Extended Data Tables 2,3, where L_{Na} and L_{Nb} are the offsets along the major and minor axis, respectively. By using a nucleus density of 1300 kg m^{-3} ([37]) and an average density for the rest of the cell of 1050 kg m^{-3} ([36]), we then also computed the distance L_W between the centre of mass and the centre of buoyancy.

Centre of hydrodynamic stress. The centre of hydrodynamic stress is the point in which the resultant of all viscous stresses exerted by the fluid on the cell (in our case of swimming cells, resulting from the combination of displacement, reorientation, and sedimentation) acts. Bodies with cylindrical symmetry have a centre of hydrodynamic stress located along the axis of symmetry[38]. To model the flow around a fore-aft asymmetric cell, we solved the three-dimensional Navier-Stokes equations around a cell with the finite element software COMSOL Multiphysics (Burlington, MA), using the characteristic size and shape determined experimentally for the upward-swimming cells (see Extended Data Table 2, and Extended Data Fig. 4) and their characteristic swimming speed (70 μm s^{-1}). Imposing the torque-free condition (sum of all torques on the cell must vanish) allowed us to determine the position of the centre of hydrodynamic stress, C_H. Specifically, the coordinates of C_H were determined by finding the minimum of the surface integral of the cross product between the stress force and the surface of the cell. The lengthscale L_H quantifies the distance between the centre of buoyancy and the centre of hydrodynamic stress.

Cell mechanics model to predict orientational stability. For a body of revolution swimming in a fluid at a low Reynolds number, there is separation of the equations for translational and rotational motion[38]. This allows us to write the force-free conditions along the major-axis and minor axis directions as

$$P \sin\varphi = D \sin\theta$$
$$P \cos\varphi - D \cos\theta = (\rho_{cell} - \rho_{fluid})\, Vg, \qquad (2)$$

where P is the propulsion force, originating from the beating of the flagellum and assumed to act along the major axis of the cell, which is φ relative to the vertical; D is the drag force, acting by definition in the centre of hydrodynamic stress C_H and directed in the opposite direction of the cell swimming velocity, which is θ relative to the vertical; V is the volume of the cell; ρ_{cell} and ρ_{fluid} are the densities of the cell and the fluid, respectively. The drag D on a spheroid moving in a fluid with dynamic viscosity η at velocity v depends on the angle $\alpha = \theta - \varphi$ between the body axis (oriented at an angle φ to the vertical) and the direction of motion (oriented at an angle θ to the vertical), and can be computed as $D = D_{\parallel} \cos\alpha + D_{\perp} \sin\alpha$ ($D_{\parallel}$ and $D_{\perp}$ are the drag forces corresponding to motion along and perpendicular to the direction of the major axis of the spheroid, respectively).

One additional equation can be derived by balancing torques around the centre of buoyancy C_B, resulting in $T_H + T_W = T_V$, where T_H is the torque generated by the drag force D, T_W is the torque generated by the weight of the cell $W = V \rho_{cell} g$, $T_V = R\eta\omega$ is the net viscous torque, R is the coefficient of resistance of the body to rotational motion, and ω is the rotation rate of the cell. The propulsion force P generates no torque about C_B, because it acts along the major axis of the cell and goes through C_B. The torque-balance equation reads

$$D \sin(\theta - \varphi)\, L_H - W [\sin\varphi - \arctan(L_{Nb}/L_{Na})]\, L_W = R\eta\omega, \qquad (3)$$

where $W\arctan(L_{Nb}/L_{Na})$ is the contribution to the gravitational torque coming from the offset $L_{Nb} = 0.25 \pm 0.26$ µm of the nucleus within the equatorial plane (Extended Data Figure 3d). For a given swimming speed v, we numerically solved (using Mathematica) the system of three equations (2) and (3) for the unknowns P, φ, and ω. This yielded the rotation rate, ω(θ), as a function of the swimming orientation to the vertical, θ. To quantify the cell stability, we then extracted the reorientation timescale B from ω(θ) through the sinusoid-fitting method described above. We note that a stability analysis for upward swimming HA452 cells (with parameters taken from Extended Data Table 2) showed that the torque $W\arctan(L_{Nb}/L_{Na})$ does not change the stability of the cell (*i.e.*, upward vs. downward; Extended Data Fig. 7c) and this torque was thus neglected in the remainder of the analysis. When solving Eqs. (2) and (3) in Mathematica we made the approximation that even for fore-aft asymmetric cells the drag can be computed as the drag on the corresponding spheroid (*i.e.*, with asymmetry coefficient set to $c = 0$), defined as the spheroid with the same volume and same aspect ratio a/b (*i.e.*, using 'equivalent semi-axes', a_{eq} and b_{eq}), because the drag for the latter is known analytically. Specifically, we have computed the drag on the most fore-aft asymmetric HA452 cell we observed ($a = 7.87$ µm, $b = 5.60$ µm, $c = 1.04$ µm; Extended Data Table 2) by solving the 3D Navier-Stokes equations around the cell in Comsol Multiphysics. We found that the drag on the fore-aft asymmetric cell exceeds the drag on the corresponding spheroid ($a_{eq} = 7.95$ µm, $b_{eq} = 5.65$ µm, $c = 0$) by only 2%, irrespective of the direction of motion (*i.e.*, for both $D_{\parallel}$ and $D_{\perp}$). The approximation of replacing the fore-aft asymmetric shape with a spheroid for drag calculations had a negligible effect on the stability of the cell (compare red and pink curves in Extended Data Fig. 7d). For a prolate spheroid, $D_{\parallel} = 6\pi\eta v r_{eq} K_{\parallel}$ and $D_{\perp} = 6\pi\eta v r_{eq} K_{\perp}$ where r_{eq} is the radius of the sphere with volume equal to the spheroid and $K_{\parallel}$ and

$K_\perp$ are shape factors, which depend on the ratio of minor over major axes of the spheroid, $t = a/b$. The shape factors are approximated[38,39] as $K_\parallel(t) = 4(t^2-1)^{3/2} / 3t^{1/3} / [(2t^2-1)^{1/2} \ln[t + (t^2-1)^{1/2} - t(t^2-1)^{1/2}]$ and $K_\perp = 8(t^2-1)^{3/2} / 3t^{1/3} / [(2t^2-3)^{1/2} \ln[t + (t^2-1)^{1/2} + t(t^2-1)^{1/2}]$. The coefficient of resistance of a prolate spheroid to rotational motion is[39] $R(t) = 2/3t\,(t^2+1)\,(t^2-1)^{3/2}/[(2t^2-1)\ln[t + (t^2-1)^{1/2}] - t(t^2-1)^{1/2}]$.

Stress quantification. To quantify the generation of nitrosative stress, cells exposed to overturning and control cells were sampled from the millifluidic chamber as described above, and incubated for 30 min in 500 nM DAF-FM Diacetate (Molecular Probes, Life Technologies), prepared by diluting the original aliquot in the cell culturing medium f/2. DAF-FM Diacetate is a chemical reagent that enables the detection of low concentrations of nitric oxide (NO), a common reactive nitrogen species (RNS) exuded by eukaryotic cells under stress[40,41] (Supplementary Information). DAF-FM by itself is not fluorescent, but forms a fluorescent benzotriazole group (ex/em = 495/515 nm) upon reaction with the free radical NO. After incubation, cells were illuminated using cyan light (ex ~495 nm) and the fluorescent readout was quantified over time using epifluorescent microscopy. For each cell, the fluorescent intensity increased over time, and reached the peak value at the onset of cell lysis. The magnitude of fluorescent intensity just before cell lysis corresponded to the maximum value of the NO accumulation in the cell. For the quantification, each measurement was first normalized with the value of maximum fluorescence intensity. The stress accumulation rates in each experiment was calculated using a linear fit on the portion of the dataset where the stress signal was higher than 10% of its maximum intensity.

Statistical tests. We performed a one-way ANOVA to test the differences in the upward bias index r between the still control and the three reorientations treatments – horizontal, vertical, and stochastic. Experiments reported in Figs. 1g and 2b,c were carried out in 4 replicates. In each replicate, more than 1000 cells were recorded within the field of view to extract the upward bias, r. Anderson-Darling test was performed to test the normality assumption in the four treatments (Control: $p = 0.28$; Horizontal: $p = 0.55$; Vertical: $p = 0.16$; Stochastic: $p = 0.39$). Bartlett's test was performed to check for homogeneity of variance ($\chi_3 = 4.39$, $p = 0.22$). We tested for multiple comparisons using a post-hoc Tukey's HSD test (Extended Data Table 1). A Kruskal-Wallis test was conducted (Bartlett's test revealed variance heterogeneity) to test the stress differences between the still control and the two subpopulations, top and bottom. Dunn's test was performed for multiple comparisons (Extended Data Table 4).

References

1. Margalef, R. Life-forms of phytoplankton as survival alternatives in an unstable environment. *Oceanologica Acta* **1,** 493–509 (1978).
2. Smayda, T. J. & Reynolds, C. S.Community assembly in marine phytoplankton: application of recent models to harmful dinoflagellate blooms. *J. Plankton Res.* **23,** 447–61 (2001).
3. Bollens, S. M., Rollwagen-Bollens, G., Quenette, J. A. & Bochdansky, A. B. Cascading migrations and implications for vertical fluxes in pelagic ecosystems. *J. Plankton Res.* **33,** 349–55 (2011).
4. Schuech, R. & Menden-Deuer, S. Going ballistic in the plankton: Anisotropic swimming behavior of marine protists. *Limnol. Oceanogr. Fluids Environ.* **4,** 1–16 (2014).
5. Sullivan, J. M., Swift, E., Donaghay, P. L. & Rines, J. E. B. Small-scale turbulence affects the division rate and morphology of two red-tide dinoflagellates. *Harmful Algae* **2,** 183–99 (2003).
6. Berdalet, E. *et al.* Species-specific physiological response of dinoflagellates to quantified small-scale turbulence. *J. Phycol.* **43,** 965–77 (2007).
7. Lozovatsky, I., Lee, J., Fernando, H.J.S, Kang, S.K., Jinadasa, S.U.P. Turbulence in the East China Sea: The summertime stratification. *J. Geophys. Res. Oceans.* **120**, 1856-71 (2015).
8. Thomas, W. H. & Gibson, C.H. Effects of small-scale turbulence on microalgae. *J. Appl. Phycol.* **2**, 71-77 (1990).
9. Sverdrup, H. On conditions for the vernal blooming of phytoplankton. *J. du Cons.* **18,** 287–95 (1953).
10. Barton, A. D., Dutkiewicz, S., Flierl, G., Bragg, J. G. & Follows, M. J. Patterns of diversity in marine phytoplankton. *Science.* **327,** 1509–11 (2010).
11. Thomas, M. K., Kremer, C. T., Klausmeier, C. A. & Litchman, E. A global pattern of thermal adaptation in marine phytoplankton. *Science.* **338,** 1085–88 (2012).
12. Brun, P. *et al.* Ecological niches of open ocean phytoplankton taxa. *Limnol. Oceanogr.* **60**, 1020–38 (2015).
13. Litchman, E. & Klausmeier, C. A. Trait-Based Community Ecology of Phytoplankton. *Annu. Rev. Ecol. Evol. Syst.* **39,** 615–39 (2008).
14. Villareal, T. A. & Carpenter, E. J. Buoyancy regulation and the potential for vertical migration in the oceanic cyanobacterium *Trichodesmium*. *Microb. Ecol.* **45,** 1–10 (2003).
15. Franks, P. J. S. Has Sverdrup's critical depth hypothesis been tested? Mixed layers vs. turbulence layers. *J. Mar. Science*. **72**, 1-11 (2015).
16. Zirbel, M. J., Veron, F. & Latz, M. I. The reversible effect of flow on the morphology of *Ceratocorys horrida*. *J. Phycol*. **58,** 46–58 (2000).
17. Yamasaki, Y. *et al.* Extracellular polysaccharide-protein complexes of a harmful alga mediate the allelopathic control it exerts within the phytoplankton community. *ISME J.* **3,** 808–17 (2009).

18. Durham, W. M., Kessler, J. O. & Stocker, R. Disruption of vertical motility by shear triggers formation of thin phytoplankton layers. *Science.* **323,** 1067–70 (2009).
19. Roberts, A. M. Geotaxis in motile micro-organisms. *J. Exp. Biol.* **53,** 687–99 (1970).
20. Durham, W. M. *et al.* Turbulence drives microscale patches of motile phytoplankton. *Nat. Commun.* **4,** 2148 (2013).
21. Thorpe, S. A. *An introduction to ocean turbulence*. Cambridge University Press (2007).
22. La Porta, A., Voth, G. A., Crawford, A. M., Alexander, J. & Bodenschatz, E. Fluid particle accelerations in fully developed turbulence. *Nature* **409,** 1017–19 (2001).
23. Hara, Y. & Chihara, M. Morphology, ultrastructure and taxonomy of the raphidophycean alga *Heterosigma akashiwo. Bot. Mag.* **100**, 151–63 (1987).
24. Smayda, T. J. Adaptations and selection of harmful and other dinoflagellate species in upwelling systems.1. Morphology and adaptive polymorphism. *Prog. Oceanogr.* **85,** 71–91 (2010).
25. Hemmersbach, R., Volkmann, D. & Hader, D. P. Graviorientation in protists and plants. *J. Plant Physiol.* **154,** 1–15 (1999).
26. Besson-Bard, A., Courtois, C., Gauthier, A., Dahan, J., Dobrowolska, G., Jeandroz, S., Pugin, A. & Wendehenne, D. Nitrix oxide in plants: production and cross-talk with Ca^{2+} signalling. *Molecular Plant* **1**, 218-228 (2008).
27. Bulmer, M. G. Selection for iteroparity in a variable environment. *Am. Nat.* **126,** 63-71 (1985).
28. Moxon E.R., Rainey P.B., Nowak M.A. & Lenski R.E. Adaptive evolution of highly mutable loci in pathogenic bacteria. *Curr Biol*. **4**, 24-33 (1994).
29. Ackermann, M. A. functional perspective on phenotypic heterogeneity in microorganisms. *Nat. Rev. Microbiol.* **13,** 497–508 (2015).
30. Guasto J.S., Rusconi R. & Stocker R. Fluid mechanics of planktonic microorganisms. *Annu. Rev. Fluid Mech.*, **44**, 373-400 (2012).

Methods References

31. Harvey, E. L., Menden-Deuer, S. & Rynearson, T. A. Persistent intra-specific variation in genetic and behavioral traits in the raphidophyte, *Heterosigma akashiwo*. *Front. Microbiol.* **6,** 1–12 (2015).
32. Foster K. & Smyth R. Light antennas in phototactic algae. *Microbiol. Rev.* **44**, 572-630 (1980).
33. Ouellette, N. T., Xu, H. & Bodenschatz, E. A quantitative study of three-dimensional Lagrangian particle tracking algorithms. *Exp. Fluids* **40,** 301–13 (2006).
34. Gurarie, E., Grünbaum D. & Nishizaki, M.T. Estimating 3D movements from 2D observations using a continuous model of helical swimming. *Bull Math Biol.* **73**, 1358-77 2011.
35. Roberts, A. M. & Deacon, F. M. Gravitaxis in motile micro-organisms: The role of fore–aft body asymmetry. *J. Fluid Mech.* **452,** 405–23 (2002).
36. Wada, M., Miyazaki, A. & Fujii, T. On the mechanisms of diurnal vertical migration

behavior of *Heterosigma akashiwo* (Raphidophyceae). *Plant Cell Physiol.* **26**, 431–6 (1985).
37. Milo, R. & Phillips, R. *Cell biology by the numbers*. Garland Science, Taylor & Francis Group, LLC, New York (2016).
38. Happel, J. & Brenner, H. *Low Reynolds number hydrodynamics: with special application to particulate media (Mechanics of fluids and transport processes)*. Volume 1, Englewood Cliffs, New Jersey (1983).
39. Koenig, S. H. Brownian motion of an ellipsoid. A correction to Perrin's results. *Biopolymers.* **14,** 2421-3 (1975).
40. Bouchard, J.N. & Yamasaki, H. Heat stress stimulates nitric oxide production in *Symbiodinium microadriaticum*: a possible linkage between nitric oxide and the coral bleaching phenomenon. *Plant Cell Physiol*. **49**, 641-52 (2008).
41. Vardi, A. *et al*. A diatom gene regulating Nitric-Oxide signaling and susceptibility to diatom-derived aldehydes. *Current Biology* **18**, 1-5 (2008).

Supplementary Information is available in the online version of the paper.

Acknowledgements. We thank Martin Ackermann for input on bet hedging, Guido Boffetta and Massimo Cencini for sharing DNS data, Susanne Menden-Deuer for providing *Heterosigma akashiwo* CCMP3107 and for insightful discussions, Elisa Berdalet, Assaf Vardi, Don Anderson and Dennis J. McGillicuddy for insightful suggestions. This work was partially supported by a Human Frontier Science Program Cross Disciplinary Fellowship (to A.S.), a Swiss National Science Foundation Early Postdoc Mobility Fellowship (to F.C.), and a Gordon and Betty Moore Marine Microbial Initiative Investigator Award (GBMF 3783, to R.S.).

Author Contributions. A.S., F.C., and R.S. designed research. A.S. and F.C. performed research and analysed data. A.S., F.C., and R.S. wrote the paper.

Author Information. Reprints and permissions information is available at www.nature.com/reprints. The authors declare no competing financial interests. Correspondence and requests for materials should be addressed to R.S. (romanstocker@ethz.ch).

FIGURES

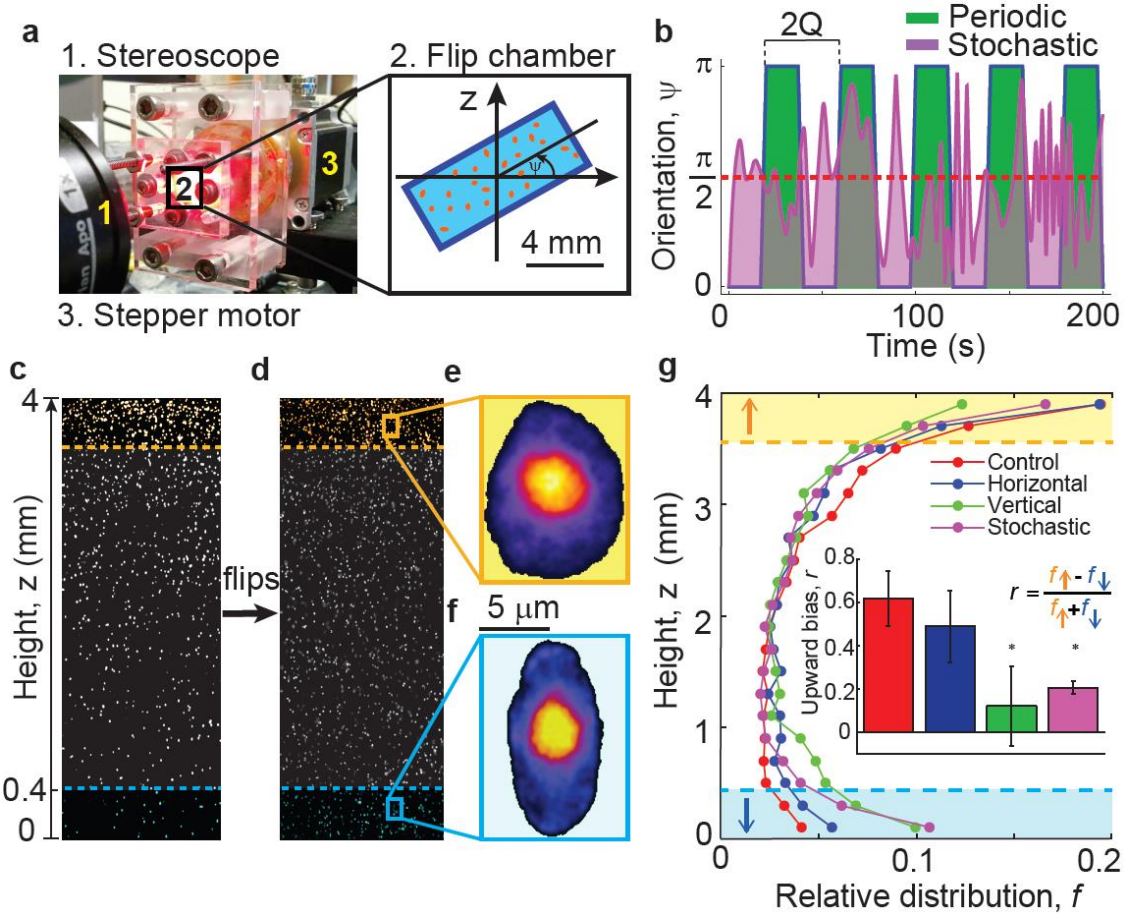

Figure 1 | Active response of HA452 to reorientations relative to gravity. (a) The automated millifluidic chamber used to expose phytoplankton cells to turbulence-like reorientations. **(b)** A square wave (green) comprising periodic reorientation events of amplitude π ('flips') and period Q = 18 s (Methods). Time series of the orientation, $\psi(t)$, of a passive particle relative to the vertical in a 3D isotropic turbulent flow (magenta), obtained from a DNS simulation. The dashed line denotes the direction of gravity vector, $\boldsymbol{g}$ ($\psi = \pi/2$). **(c,d)** Equilibrium distribution of HA452 over the height of the chamber, **(c)** before and **(d)** after 100 flips (30 min). Hued regions extend 400 μm from the top (↑, orange) and bottom (↓, blue) of the chamber. **(e,f)** False-colour epifluorescence micrographs of HA452 cells harvested from **(e)** the top and **(b)** the bottom of the chamber, after 30 min of flipping in the vertical plane (period Q = 18 s). **(g)** Equilibrium distributions of cells over the chamber height upon different treatments, each lasting 30 min: still conditions (control, red), periodic flips in the horizontal plane (horizontal, blue; Q = 18 s), periodic flips in the vertical plane (vertical, green; Q = 18 s), and continuous, stochastic reorientations (stochastic, magenta). For each case, the equilibrium vertical distribution was measured 30 min after treatment ended. **(g, inset)** The upward bias, $r = (f_\uparrow - f_\downarrow) / (f_\uparrow + f_\downarrow)$, for each treatment, where $f_\uparrow$ and $f_\downarrow$ are the relative number of cells in the top and the bottom 400 μm of the chamber (mean ± s.d. of 4 replicates, Extended Data Table 1).

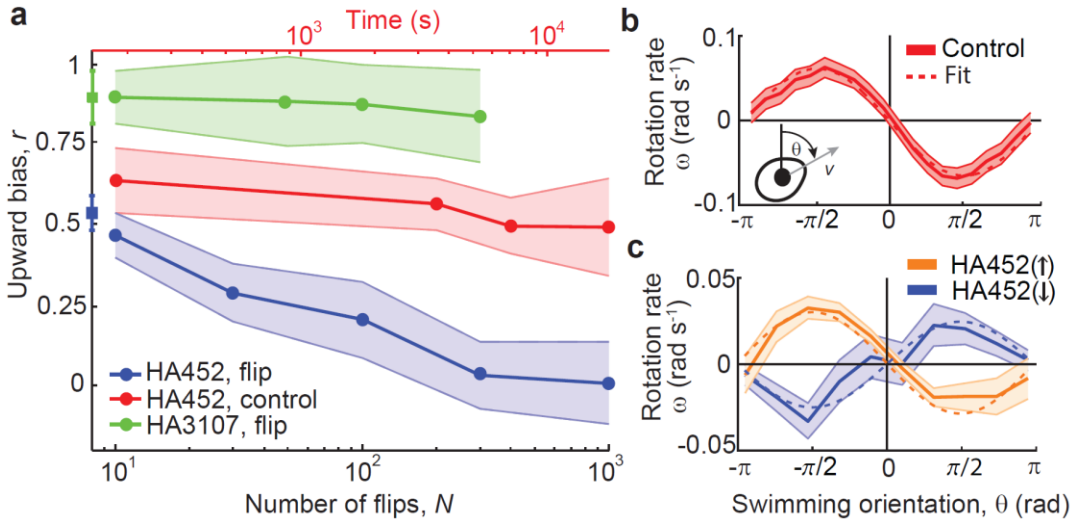

Figure 2 | Two behaviourally distinct subpopulations of HA452 rapidly emerge upon reorientation relative to gravity. (a) Upward bias, *r*, as a function of the number of flips, *N* (period *Q* =18 s, red axis denotes the equivalent time elapsed, *t* = *NQ*). For each case, the equilibrium vertical distribution was measured 30 min after treatment ended. Square symbols correspond to pre-treatment conditions, measured 30 min after filling the chamber for HA452 (blue) and HA3107 (green). Flipping induces the emergence of two subpopulations having distinct migration behaviours in HA452 (colour coded in blue, mean ± s.d. of 4 replicates), as compared to the control (cells maintained in the chamber under still conditions for the same amount of time, see red axis on top for the time conversion). Flipping does not affect HA3107 (green). **(b,c)** Rotation rate, ω(θ), of HA452 cells, as a function of the cell orientation to the vertical, θ, measured **(b)** before (*n* = 2257) and **(c)** after 30 min of flipping in the vertical plane (period *Q* = 18 s). Note that, after flipping, HA452(↑) (*n* = 1421) and HA452(↓) (*n* = 1138) subpopulations have opposite stability.

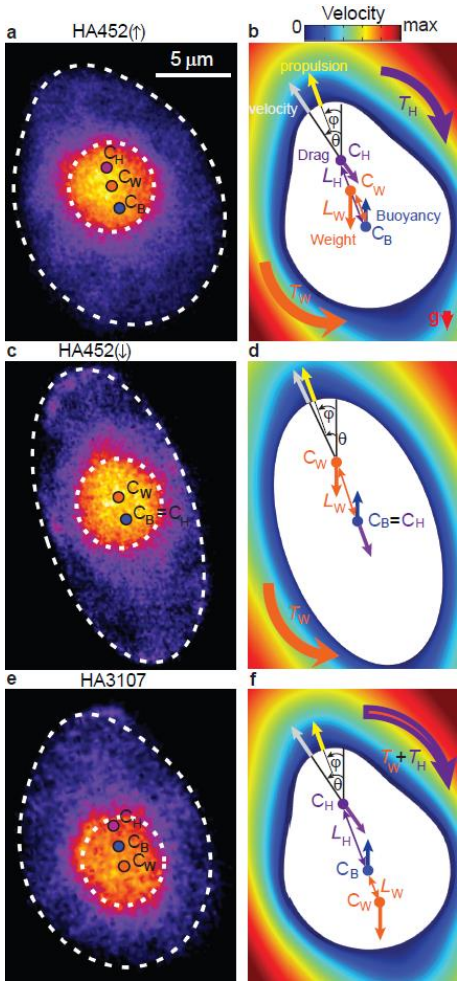

Figure 3 | A change in morphology underpins the emergence of a downward swimming subpopulation in HA452. (a,c,e) False-colour epifluorescence micrographs of HA452(↑), HA452(↓) subpopulations, and of HA3107. White dashed lines denote the contour of cell body and nucleus (bright orange). C_W, C_B, and C_H are the centres of mass, buoyancy, and hydrodynamic stress, respectively. **(b,d,f)** Free body diagrams showing the forces acting on the cell overlaid on the numerically computed flow field around the cell (not to scale). The swimming direction θ is set by the competition between the gravitational torque T_W and the hydrodynamic torque T_H about C_B. (**b**) HA452 cells collected from the top of the chamber after 30 min of flipping are top-heavy (C_W above C_B) and fore-aft asymmetric (C_H above C_B), thus T_W and T_H act in opposition. (**d**) HA452 cells collected from the bottom of the chamber after 30 min of flipping are fore-aft symmetric (C_H coincides with C_B and thus T_H vanishes) and top-heavy (C_W above C_B), so that T_W causes cells to orient downwards. (**f**) HA3107 cells are bottom-heavy (C_W below C_B) and fore-aft asymmetric (C_H above C_B), thus both T_W and T_H act to right cells up.

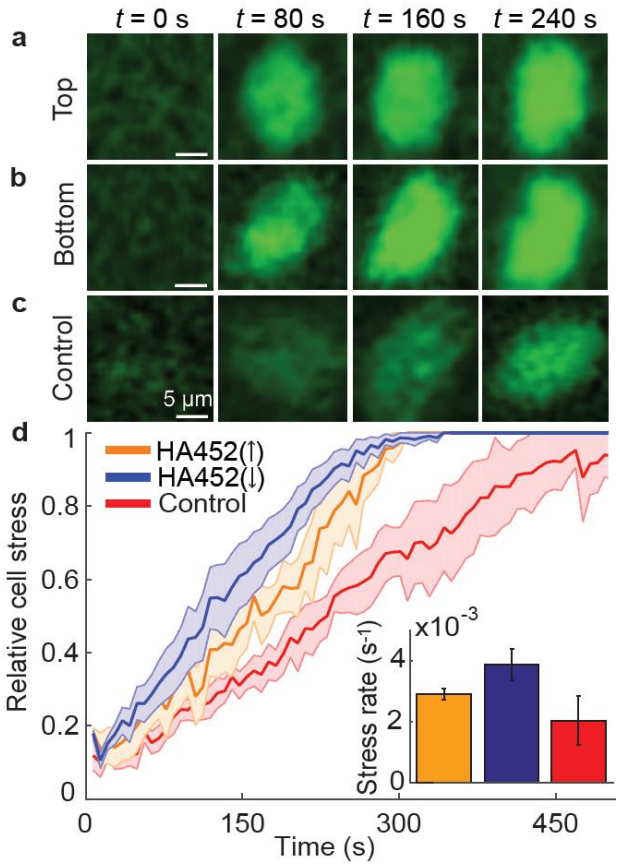

725
726

727 **Figure 4 | Reorientations relative to gravity trigger stress response in HA452. (a-c)**
728 Fluorescence intensity, measuring production of NO in cells collected from **(a)** the top
729 (subpopulation HA452(↑), n = 4), and **(b)** the bottom (subpopulation HA452(↓), n = 7) of the
730 chamber, in both cases after 30 min of flipping, as well as **(c)** cells not exposed to flipping
731 (control, n = 3). **(d)** Time series of stress accumulation, quantified as NO production
732 (Supplementary Information), for the same three cases. Solid lines denote the arithmetic
733 mean over all cells and the shaded regions represent ± 1 s.d. from the mean (see legend for
734 colour-coding). Time represents the acquisition time under the microscope. **(d, inset)** Rate of
735 stress accumulation (a multiple comparison analysis is reported in Extended Data Table 4).

736

EXTENDED DATA TABLES AND FIGURES

Extended Data Table 1 | Multiple comparisons analysis (Tukey's HSD test) between the control and the different reorientation treatments. Control = still conditions, Horizontal = flipping in the horizontal plane, Vertical = flipping in the vertical plane, Stochastic = continuous stochastic reorientations obtained from the DNS model (Methods).

Treatment comparison	Mean difference (95% confidence interval)	p-value
Control, Horizontal	0.127 (-0.167, 0.420)	0.591
Control, Vertical	0.495 (0.201, 0.789)	0.001
Control, Stochastic	0.409 (0.115, 0.703)	0.011
Horizontal, Vertical	0.368 (0.074, 0.662)	0.007
Horizontal, Stochastic	0.282 (-0.011, 0.576)	0.066
Vertical, Stochastic	-0.086 (-0.380, 0.208)	0.591

Extended Data Table 2 | *H. akashiwo* single-cell parameters for strains HA452 (subpopulations HA452(↑) and HA452(↓)) and HA3107 after 30 min of flipping, aggregated over all cells for each population. The cell contour was fitted using Eq. 1, where a is the semi-major axis, b is the semi-minor axis, c captures the degree of fore-aft asymmetry, s_N is the radius of the nucleus, L_N is the distance between the centre of the nucleus and the centre of buoyancy (positive when the former is above the latter), L_W is the distance between the centre of mass and the centre of buoyancy (positive when the former is above the latter), and B is the reorientation timescale (positive for upward stable cells Highlighted in bold are the parameters that significantly differ between the two subpopulations, HA452(↑) and HA452(↓). All data are given as mean ± s.d.. Values for individual cells ($n_{HA452(\uparrow)} = 13$, $n_{HA452(\downarrow)} = 10$, $n_{HA3107} = 12$) are given in Extended Data Table 3. Notice the minus sign in the value of B of HA452 for cells collected from the bottom of the chamber, from the subpopulation HA452(↓), signifying opposite orientational stability compared to HA452 collected from the top, from the subpopulation HA452(↑) (Methods).

Strain	a (µm)	b (µm)	c (µm)	s_N (µm)	L_N (µm)	L_W (µm)	B (s)
HA452(↑)	7.87±1.25	5.60±0.55	**1.04±0.38**	2.34±0.33	0.41±0.58	0.03±0.04	19.3±13.5
HA452(↓)	9.10±1.44	5.86±0.91	**0.18±0.24**	2.61±0.48	0.61±0.53	0.04±0.04	-23.1±10.2
HA3107	6.58±1.00	4.90±0.42	0.77±0.20	1.94±0.26	-0.42±0.26	-0.02±0.02	4.9±1.5

Extended Data Table 3 | *H. akashiwo* single-cell parameters for strains HA452 and HA3107 after 30 min of flipping, for each individual cell analysed. HA452(↑) and HA452(↓) indicate HA452 cells harvested from the top and the bottom of the chamber, respectively. See caption of Extended Data Table 2 for other details.

Cell #	Population	*a* (µm)	*b* (µm)	*c* (µm)	s_N (µm)	L_N (µm)	L_W (µm)
1	HA452(↑)	7.10	5.23	0.90	2.57	0.58	0.06
2	HA452(↑)	7.43	5.82	1.20	2.87	0.31	0.02
3	HA452(↑)	6.38	5.03	1.40	2.07	-0.11	0.01
4	HA452(↑)	8.60	6.57	1.45	2.63	0.58	0.02
5	HA452(↑)	7.88	6.05	1.75	2.24	0.88	0.03
6	HA452(↑)	7.72	4.90	1.00	2.25	0.51	0.03
7	HA452(↑)	6.80	5.20	0.75	2.25	0.52	0.03
8	HA452(↑)	9.52	5.82	0.60	2.92	1.49	0.11
9	HA452(↑)	8.41	5.40	0.40	2.22	-0.87	-0.04
10	HA452(↑)	6.38	4.94	1.00	1.76	-0.22	-0.01
11	HA452(↑)	9.59	6.28	1.50	2.43	0.33	0.01
12	HA452(↑)	7.30	5.56	0.90	2.13	0.52	0.02
13	HA452(↑)	10.28	6.32	0.90	2.07	0.84	0.02
14	HA452(↓)	8.35	7.00	0.50	3.38	1.38	0.11
15	HA452(↓)	9.82	5.13	0.20	2.65	0.76	0.05
16	HA452(↓)	8.97	4.84	0.20	2.33	1.17	0.09
17	HA452(↓)	8.38	5.66	-0.20	2.21	0.21	0.01
18	HA452(↓)	7.40	5.49	0.50	2.28	-0.34	-0.02
19	HA452(↓)	8.96	6.15	-0.20	3.05	0.01	0.00
20	HA452(↓)	10.57	5.72	0.20	2.15	0.97	0.03
21	HA452(↓)	8.12	5.44	0.20	2.15	0.71	0.04
22	HA452(↓)	8.12	5.34	0.30	2.59	0.66	0.06
23	HA452(↓)	12.27	7.81	0.10	3.32	0.53	0.03
24	HA3107	7.28	5.22	0.50	2.45	-0.65	-0.05
25	HA3107	6.38	4.97	1.00	1.61	-0.28	-0.01
26	HA3107	5.53	4.71	0.90	1.90	-0.25	-0.01
27	HA3107	6.64	4.97	0.40	1.90	-0.56	-0.02
28	HA3107	5.69	4.96	0.70	2.27	-0.18	-0.01
29	HA3107	6.90	4.64	0.60	2.20	-0.15	-0.01
30	HA3107	7.04	4.75	0.85	2.52	-0.82	-0.08
31	HA3107	5.16	3.82	0.75	1.82	-0.84	-0.05
32	HA3107	8.35	5.26	0.95	2.02	-0.63	-0.02
33	HA3107	5.66	4.87	0.70	1.42	-0.15	-0.00
34	HA3107	8.06	5.43	1.00	0.94	-0.39	-0.00
35	HA3107	6.30	5.23	0.90	2.26	-0.18	-0.01

Extended Data Table 4 | Multiple comparisons analysis (Dunn's test) of the rate of stress accumulation between the cells from control and cells collected from the top and the bottom of the millifluidic chamber (belonging to subpopulations HA452(↑), HA452(↓) respectively) after 30 min of flipping. Control = still conditions; HA452(↑) = HA452 cells collected from the top of the chamber upon flipping; HA452(↓) = HA452 cells collected from the bottom of the chamber upon flipping ($n_{HA452(\uparrow)} = 4$, $n_{HA452(\downarrow)} = 7$, $n_{Control} = 3$).

Treatment comparison	Mean difference (95% confidence interval)	p-value
Control, HA452(↑)	-5.25 (-12.88, 2.38)	0.272
Control, HA452(↓)	-8.00 (-14.89, -1.11)	0.017
HA452(↓), HA452(↑)	-2.75 (-9.01, 3.51)	0.652

Extended Data Table 5 | The response of different phytoplankton species to flipping. The vertical distribution of the population is expressed in terms of the upward bias, *r*, for the control and after 300 flips ($r > 0$ denotes upward accumulation, $r < 0$ denotes downward accumulation, and $r \sim 0$ denotes a symmetric distribution). Subscript "RCC" denotes species acquired from the Roscoff Culture Collection; all other species were acquired from CCMP (Culture Collection of Marine Phytoplankton; currently: National Center of Marine Algae and Microbiota). In the column "Class", "R" indicates Raphidophyceae and "D" Dinophyceae. An asterisk indicates that the difference between the flip treatment and the control is statistically significant (in particular, for the two additional species that exhibited a split: CM2962: $t_6 = 3.66$, $p = 0.01$; PM291: $t_4 = 2.85$, $p = 0.04$). The last column provides a qualitative description of the behavioural response to the flips.

Strain	Strain No.	Class	Upward bias, *r* control	Upward bias, *r* 300 flips	Behavioural response
Heterosigma akashiwo	HA452	R	0.55	0.15*	**split**
Heterosigma akashiwo	HA3107	R	0.86	0.85	no effect
Heterosigma akashiwo	HA3374	R	0.67	-0.52	up do down
Fibrocapsa japonica_cf	FJ2965	R	0.93	0.94	no effect
Chattonella sp	CSP218	R	0.60	0.51	no effect
Chattonella marina_cf	CM2962	R	0.86	-0.01*	**split**
Chattonella subsalsa	CS2814	R	0.72	-0.79	up to down
Akashiwo sanguinea	$AS3040_{RCC}$	D	0.94	0.51	no effect
Alexandrium tamarense	AT1771	D	-0.44	-0.99	no effect
Alexandrium tamarense	AT2023	D	0.45	0.43	no effect
Alexandrium tamarense	AT1598	D	-0.97	-0.92	no effect
Alexandrium tamarense	$AT4087_{RCC}$	D	0.94	-0.30	up to down
Karenia brevis	KB2281	D	0.33	0.75	strongly up
Karenia brevis	KB2229	D	0.25	0.88	strongly up
Prorocentrum minimum	PM699	D	-0.28	-0.40	no effect
Prorocentrum minimum	PM696	D	0.82	0.75	no effect
Prorocentrum minimum	$PM291_{RCC}$	D	0.88	0.08*	**split**

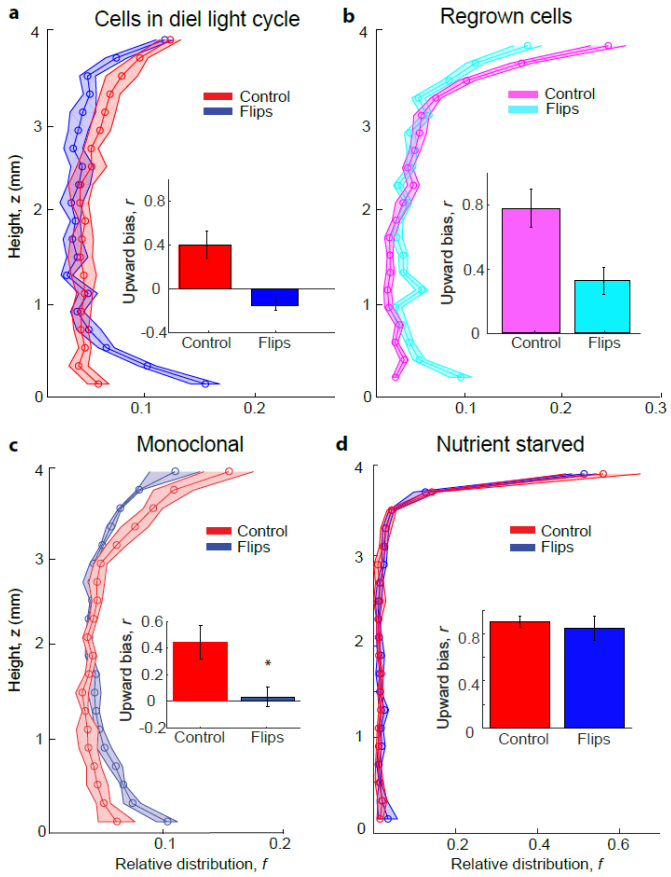

Extended Data Figure 1 | Vertical distribution of HA452 cells for (a) a population grown under a diel light cycle, (b) for regrown cells, (c) for a monoclonal population, and (d) for a starved population. (**a**) Upward bias for exponential-phase HA452 cells grown under a diel light cycle (14 h light / 10 h dark), showing the characteristic split after 100 flips (blue curve; red curve is control). Note that a similar split was observed for cells cultured under constant illumination (Fig. 1g). (**b**) Cells regrown from those collected from the bottom of the chamber after 100 flips. Although cells collected from the bottom were positively gravitactic (swimming downwards; blue curve in panel a), cells regrown from these are negatively gravitactic (swimming upwards; pink curve in panel b). Upon exposure to 100 flips, these regrown cells again exhibited the population split (cyan curve). (**c**) The population split also occurs in a monoclonal population of HA452. The inset shows the upward bias calculated from the relative distribution of the cells at equilibrium, after being exposed to 100 flips (blue) and for the control (red). The star indicates statistical significance in the difference between treatment and control ($t_4 = 4.79$, $p = 0.009$). (**d**) A nutrient-starved HA452 population does not split upon flipping. Nutrient-starved cells were harvested at stationary phase (350 h after inoculation). For all panels, insets show the upward bias for the different treatments. All the experiments have been carried out in 3 replicates.

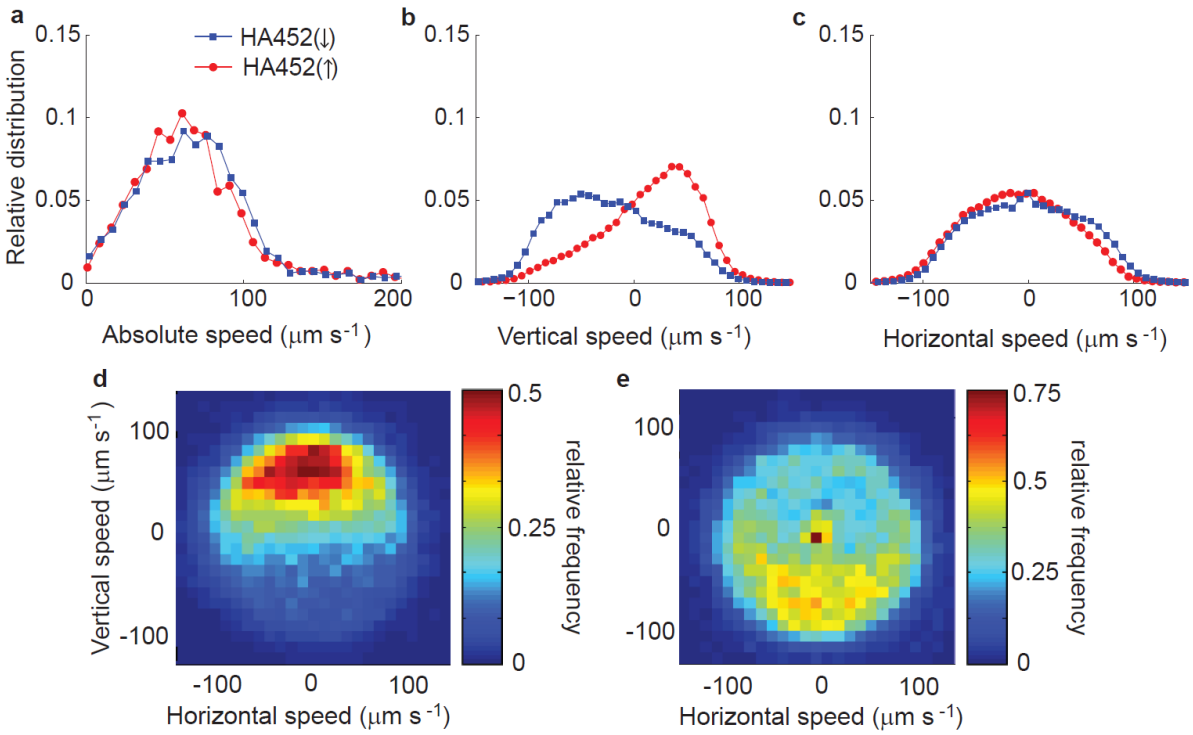

807

808 **Extended Data Figure 2 | Swimming behaviour of HA452 cells after exposure to 100**
809 **flips. (a)** The relative distribution of swimming speeds, obtained by image analysis of cells in
810 the flipping chamber, showing no difference in the absolute swimming speed of the two
811 subpopulations, HA452(↑) and HA452(↓). **(b)** Distribution of the vertical component of the
812 swimming velocity in HA452(↑) and HA452(↓), showing distinct peaks in opposite
813 directions, at approximately ±50 μm s^{-1}, and corresponding to upward and downward
814 swimming, respectively. **(c)** Distribution of the vertical component of the swimming velocity
815 in HA452(↑) and HA452(↓), showing no appreciable difference between the two
816 subpopulations. In all panels, speeds were obtained by tracking cells for 15 s just after a
817 single flip that was additional to the 100 flips. Here, trajectories in the top 1 mm of the
818 chamber were assigned to HA452(↑) and trajectories in the bottom 1 mm were assigned to
819 HA452(↓). For each subpopulation, velocities were averaged over all trajectories. **(d-e)** The
820 joint distribution of the swimming velocity along the vertical and horizontal directions for
821 HA452(↑) and HA452(↓). The colour bar indicates the number of cell trajectories counted
822 over the 15 s movie normalized by the number of cells in each subpopulation.

823

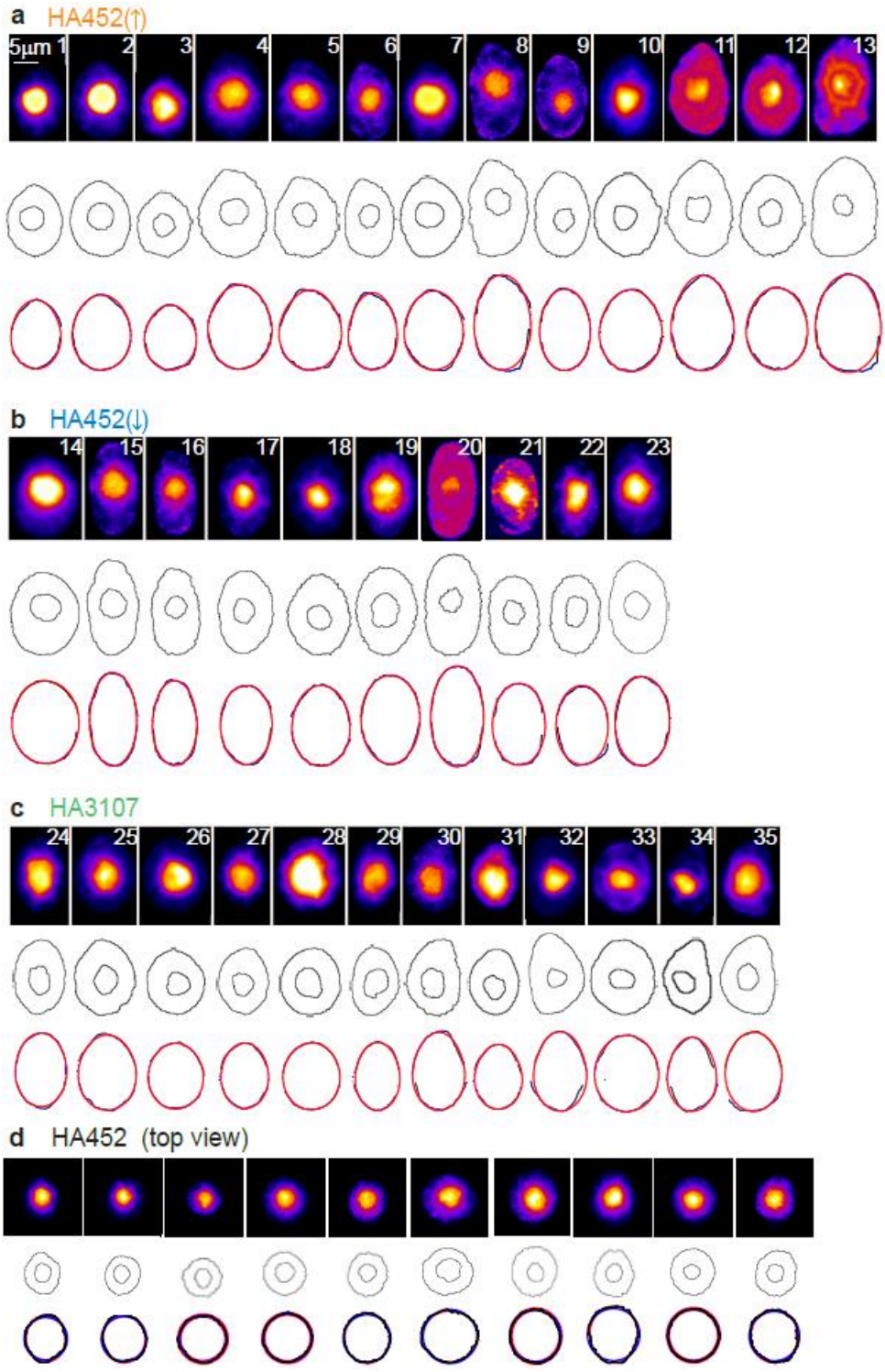

824

825 **Extended Data Figure 3 | Quantification of the shape and nucleus position of *H.***
826 ***akashiwo* cells based on single-cell microscopy, for subpopulations HA452(↑), and**
827 **HA452(↓), as well as strain HA3107. (a,c)** The upper row in each panel shows micrographs
828 obtained by epifluorescence microscopy (Methods), respectively of (**a**) HA452 cells
829 harvested from the top (HA452(↑), *n* = 13) and (**b**) bottom (HA452(↓), *n* = 10) of the
830 millifluidic chamber after 100 flips, and of (**c**) HA3107 (*n* = 12). The cell itself was
831 visualized using an inverted microscope (Nikon TE2000) in phase contrast, equipped with a

20× or 40× objective and an Andor iXon Ultra 897 camera. Prior to imaging, cells were stained with SYTO 9 (Methods) to visualize the nucleus through fluorescence microscopy (central bright spot). Image analysis was used to extract the contour of each cell and the position of its nucleus (middle rows). Experimentally obtained cells contours (black) were fitted with a 3-parameter curve (Eq. 1; red) (lower rows). Single-cell parameters associated with these fits are given in Extended Data Tables 2 and 3. (**d**) Quantification of the axial-symmetry of HA452 cells from single-cell microscopy. The upper row shows micrographs obtained by epifluorescence microscopy for 10 cells. Image analysis was used to extract the contour of each cell and the position of its nucleus (middle row). Experimentally obtained cells contours (black) were fitted with (i) an ellipse with major and minor semi-axis b_x, b_y (red) and a circle of radius r_{eq} (blue). The degree of axial-asymmetry, quantified as $R = b_x / b_y = 1.08 \pm 0.06$ (average ± s.d., $n = 10$), was very close to that of a circle ($R = 1$), showing that cells were very close to axially symmetric. The offset of the position of the nucleus compared to the center of the circle in the plane perpendicular to the major axis was found $L_{Nb} = 0.25 \pm 0.26$ µm.

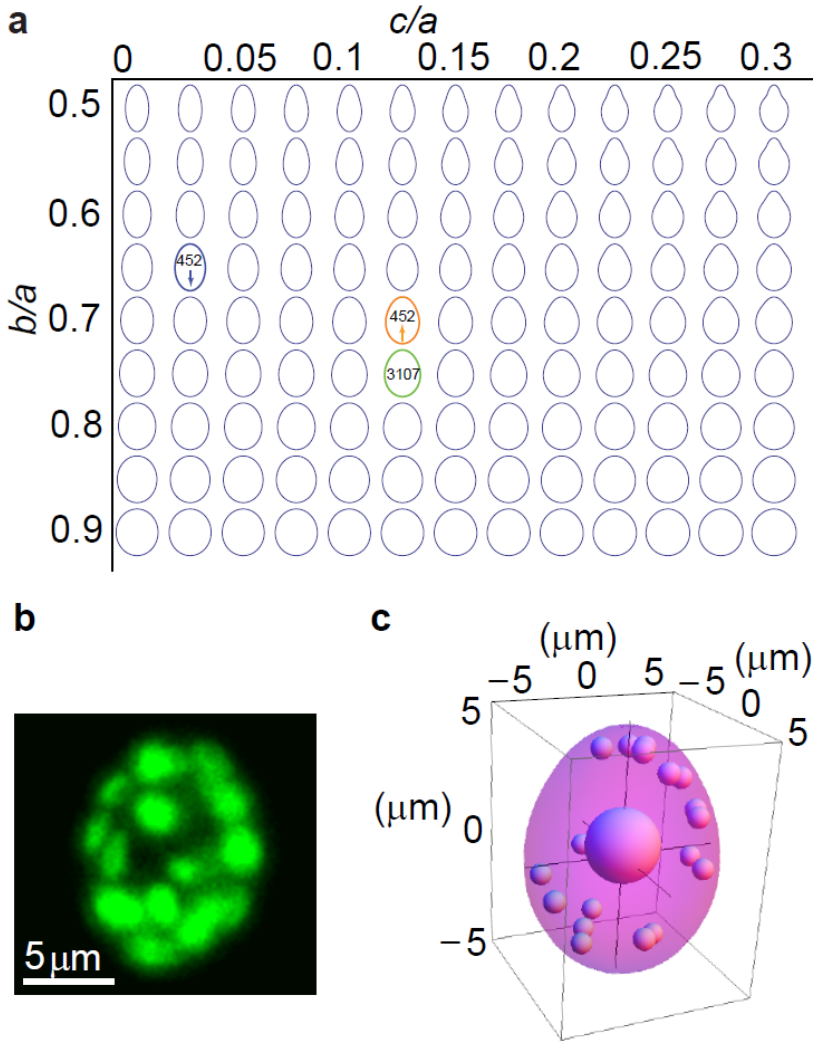

Extended Data Figure 4 | Cell shapes for HA452(↑), HA452(↓) and HA3107. (a) The graph shows the cells' shape variation in terms of the degree of fore-aft asymmetry and major/minor axis ratio (see Eq. 1). The parameter *c* denotes the degree of fore-aft asymmetry, *a* is the semi-major axis, *b* is the semi-minor axis. We highlighted the average contours (see Extended Data Table 2) for the subpopulation of downward swimmers (HA452(↓), blue), the subpopulation of upward swimmers (HA452(↑), orange), and HA3107 (green). Values of *a*, *b* and *c* are given in Extended Data Tables 2 and 3. (**b**) Epifluorescence micrographs showing the chloroplasts. (**c**) Three-dimensional schematic of a HA452 cell used to compute the contribution of chloroplasts to the offset of the center of mass relative to the contribution of the nucleus. The large blob represents the nucleus (density ρ_N = 1300 kg m^{-3}, radius s_N = 2.5 µm) and the 20 small blobs represent the chloroplasts (density ρ_{chlo} = 1150 kg m^{-3}, radius r_{chlo} = 0.75 µm), which for the purpose of computing the contribution to the center of mass were taken to be randomly distributed adjacent to the cell membrane. The contribution of the chloroplasts to the offset of the center of mass from the center of buoyancy was found to be <4% of the contribution of the nucleus and was thus neglected in the stability analysis.

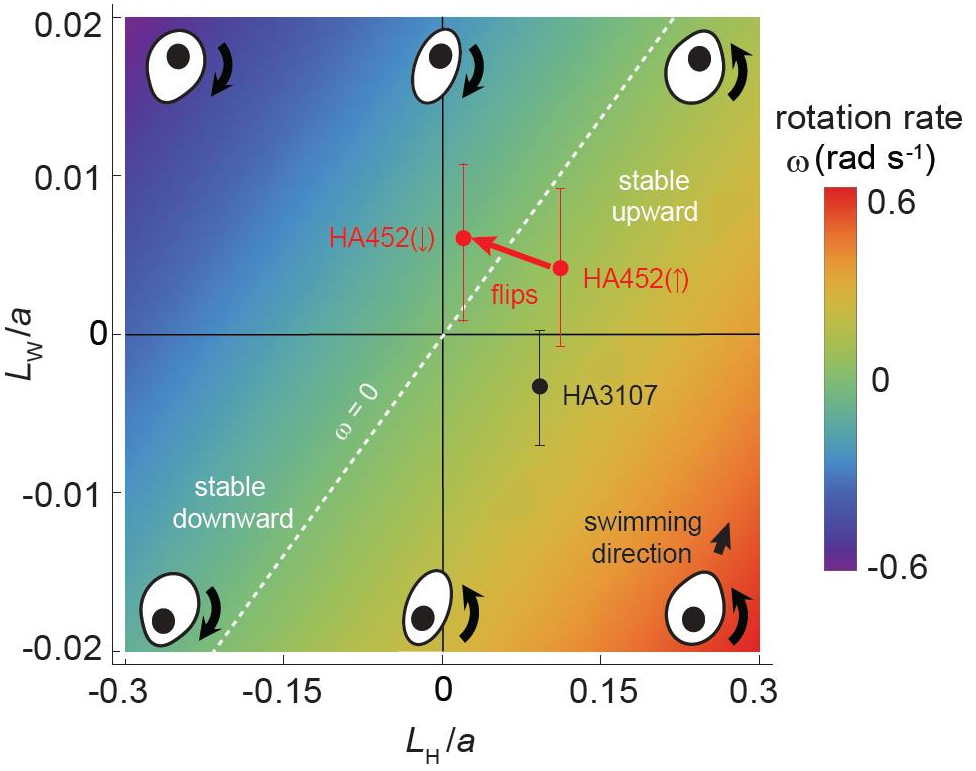

865

866 **Extended Data Figure 5 | Regime diagram of cell stability.** Two physical features –
867 summarized by two morphological length scales – determine cell stability: the asymmetry in
868 shape, quantified by L_H/a, and the mass distribution, quantified by L_W/a, where a is the semi-
869 major axis, L_H quantifies the distance between the centre of buoyancy and the centre of
870 hydrodynamic stress and L_W the distance between the centre of buoyancy and the centre of
871 mass (Fig. 3). Colours denote the cell rotation rate ω following an orientational perturbation
872 (Eq. 3): $\omega > 0$ denotes negatively gravitactic cells (stable upward), $\omega < 0$ denotes positively
873 gravitactic cells (stable downward), and $\omega = 0$ (white dashed line) denotes neutrally stable
874 cells. Sample asymmetry configurations corresponding to different locations on the regime
875 diagram are illustrated by the black-and-white schematics. Full circles denote experimental
876 data (see Extended Data Table 2). The morphological adaptation of HA452 cells in response
877 to overturning causes the population stability to switch (red arrow crossing the white dashed
878 line). The original population splits into a subpopulation swimming downward HA452(↓)
879 and a subpopulation swimming upward, HA452(↑).

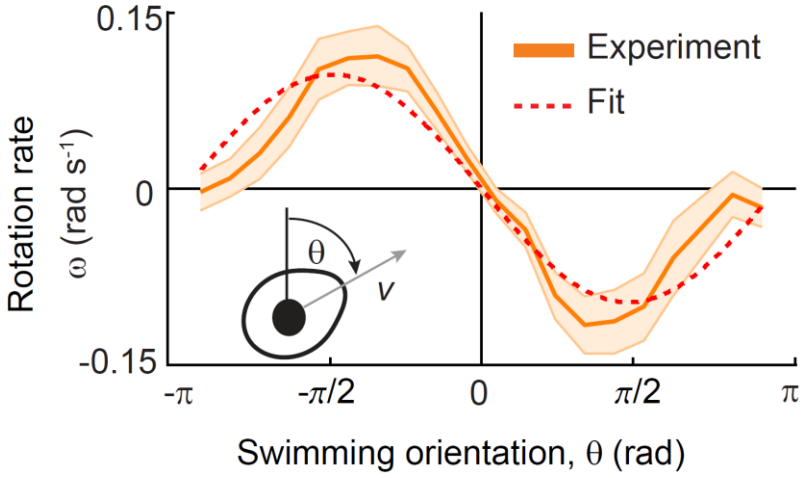

Extended Data Figure 6 | Rotation rate, ω, of HA3107 cells before the overturning treatment, as a function of the direction, θ, of the instantaneous swimming velocity, *v*, relative to the vertical. The rotation rate was quantified by tracking cells for 15 s after a single flip and averaged over all cells as a function of θ. The dashed line is a sinusoidal fit to the data used to obtain the reorientation timescale *B*. Shading denotes the standard deviation around the mean. The reorientation timescale obtained for HA3017 from these data was *B* = 4.9 s (see "Quantification of cell stability" in Materials and Methods).

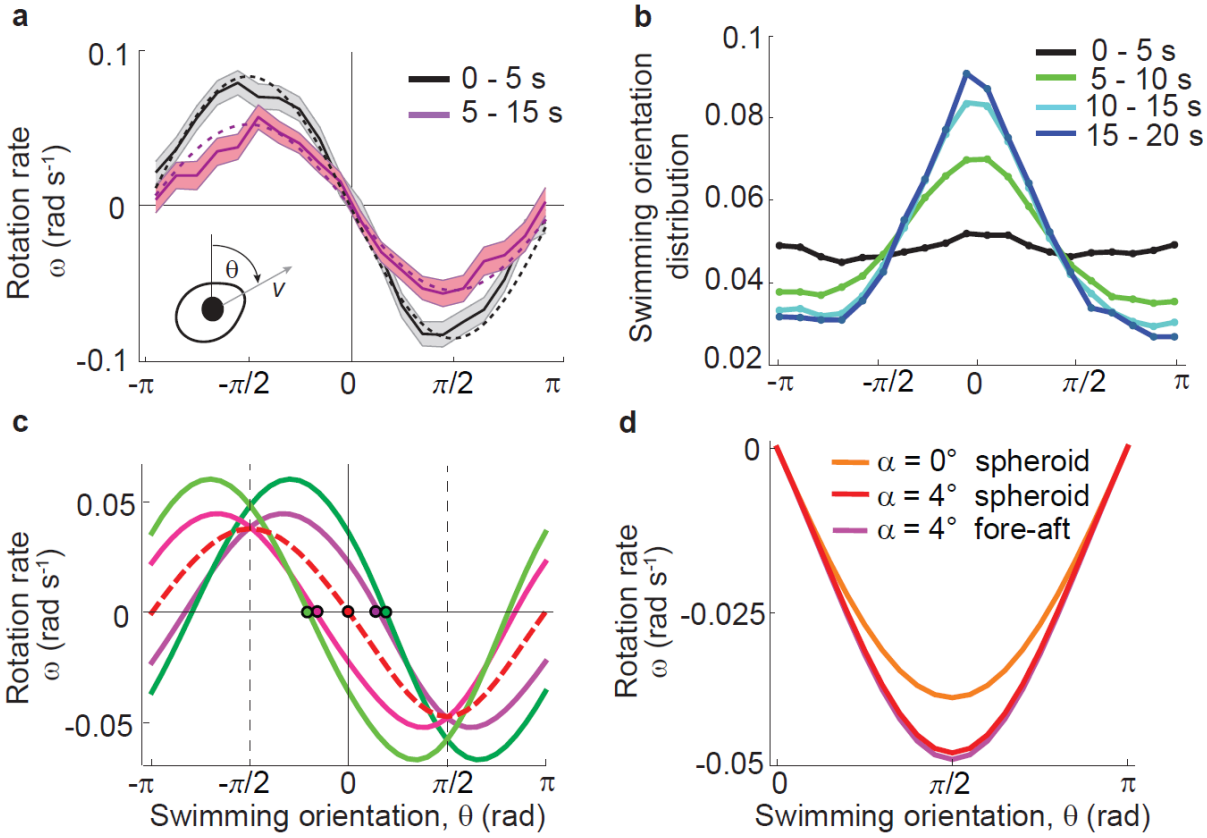

Extended Data Figure 7 | Heterogeneity in orientational stability within a HA452 population. (a) Rotation rate, ω, of HA452 cells before the overturning treatment, as a function of the direction, θ, of the instantaneous swimming velocity, *v*, relative to the vertical. The rotation rate of the cells was quantified by tracking them in the time intervals 0–5 s (grey) and 5–15 s (magenta) just after a single flip, and averaged over all the cells as a function of θ. The difference between the two curves denotes the presence of cells that reorient more rapidly and others that reorient more slowly. Dashed lines are sinusoidal fits to the experimental data, used to obtain the reorientation timescale *B*. The shading region denotes the standard error around the mean. The reorientation timescale obtained from these data are B = 7.2 s for the first 5 s and B = 12.2 s for the following 10 s, denoting a nearly two-fold higher stability for cells that were observed reorienting in the first 5 s. **(b)** Angular distribution of swimming orientation of HA452 cells before the overturning treatment. The distribution was quantified by tracking cells in the time intervals 0–5 s (black), 5–10 s (green), 10–15 s (cyan), 15–20 s (blue), just after a single flip, and averaged over all cells as a function of θ. Note that after 15 s the distribution does not appreciably change, because by that time after the flip almost all cells swim aligned along the vertical direction. The mean reorientation timescale for HA452 is B = 10.4 s. (**c**) Effect of the torque generated by the offset L_{Nb} of the nucleus within the equatorial plane, shown in terms of its effect on the dependence of the rotation rate on the body axis angle for the upward swimming subpopulation HA452(↑). The dashed red line denotes the case without offset (L_{Nb} = 0), the purple and pink lines represent the cases in which the nucleus is offset by L_{Nb} = +0.25 μm

and by L_{Nb} = -0.25 μm, respectively (the average offset measured experimentally; see Extended Data Fig. 3d) and the dark green and light green lines represent the cases in which the offset corresponds to mean+s.d. of the experimentally measured values, *i.e.*, L_{Nb} = +(0.25+0.26) = +0.51 μm and L_{Nb} = -(0.25+0.26) = -0.51 Note that the overall upward stability of the cells remains unchanged when one accounts for the effect of L_{Nb}, since the stable points for all the cases (coloured dots) always occur for a swimming orientation θ that is smaller than ±π/2 (dashed vertical lines), which separates upward and downward swimming (θ = ±28° for L_{Nb} = ±0.25 μm; θ = ±35° for L_{Nb} = ±0.51 μm. Note that the results are symmetric around the vertical direction, θ = 0°). (**d**) Stability analysis demonstrating that two assumptions made in our calculations have negligible consequences, in particular the assumptions that (i) the angle α between the body axis and the direction of motion is zero (compare orange and red lines), and (ii) the drag on the fore-aft asymmetric upward swimmers can be approximated by the drag on a spheroid (compare red and pink lines). Shown is the rotation rate as a function of body axis angle for three cases: a spheroidal cell in which the major axis is aligned with the direction of motion (α = 0, orange), a spheroidal cell in which the misalignment between major axis and direction of motion is accounted for (α = 4 degrees, red), and a fore-aft asymmetric cell in which the misalignment between major axis and direction of motion is accounted for (α = 4 degrees, pink). Parameters were taken from Extended Data Table 2 (first row), for the upward swimming cells. The fore-aft asymmetric case was simulated with Comsol Multiphysics. Note that the cell stability is the same in all three cases, as evidenced from the fact that the curve has a stable point at a swimming angle of ϕ = 0 and a negative minimum at ϕ = π/2, which together imply upward stability. Throughout our analysis, we have thus adopted the spheroidal approximation for the calculation of the drag, and took into account the contribution to the cell stability by the angle α.

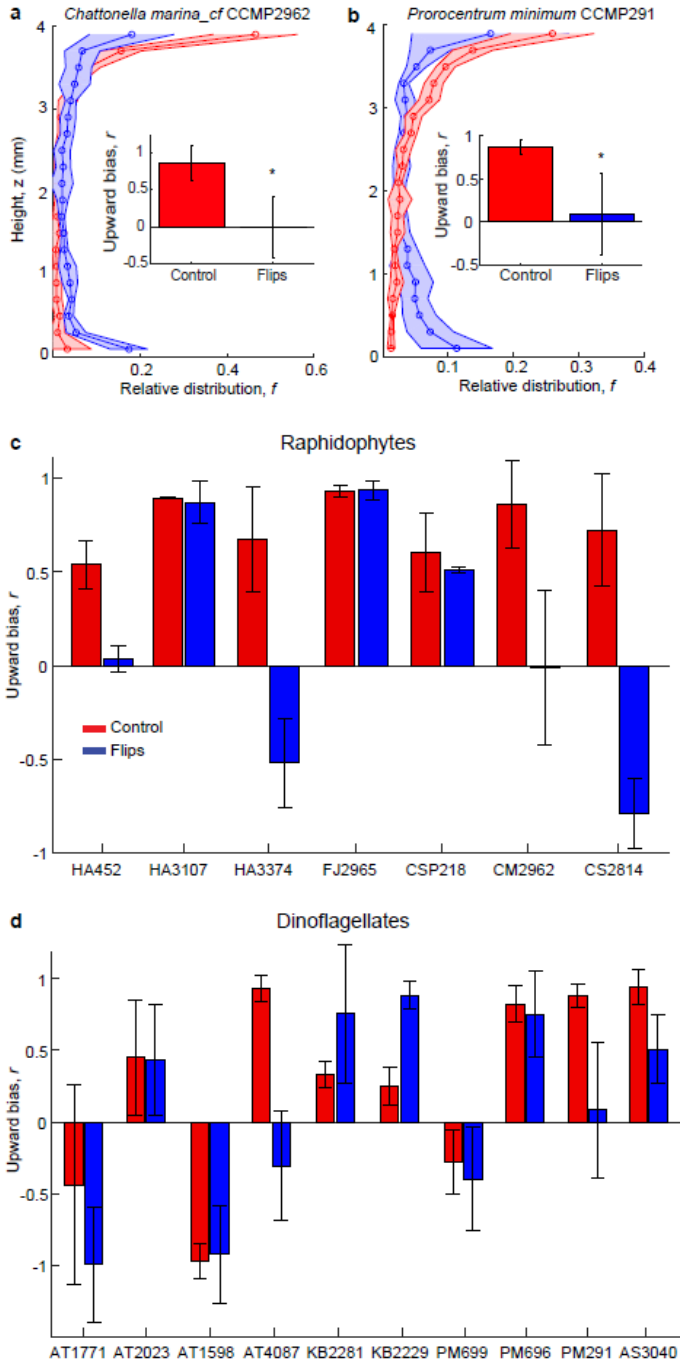

938

939 **Extended Data Figure 8 | Additional flipping experiments with a range of raphidophyte**
940 **and dinoflagellate species revealed that rapid behavioural responses in phytoplankton**
941 **to flipping are not restricted to HA452**. (**a**) Vertical distribution of *Chattonella marina_cf*
942 CCMP2962 and (**b**) *Prorocentrum minimum* CCMP291, both showing a split similar to that
943 of HA452. Insets show the upward bias, *r*, after 300 flips and for the control (same time in
944 chamber, without flipping) (mean ± s.d. of at least 3 replicates). The star indicates statistical
945 significance between the two treatments (CM2962: $t_6 = 3.66$, $p = 0.01$; PM291: $t_4 = 2.85$, $p =$
946 0.04). (**c**,**d**) Upward bias index, *r*, for (c) 7 raphidophyte strains and (d) 10 dinoflagellate
947 strains. Full names of strais are provided in Extended Data Table 5. Many of these strains
948 showed a moderate to strong response to flipping, as shown by the change in their upward
949 bias between treatment and control.

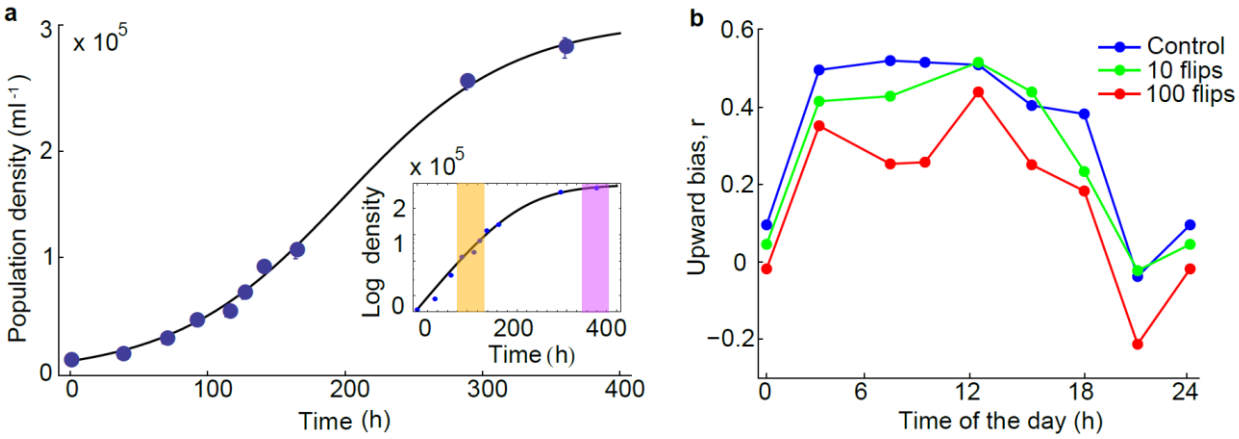

Extended Data Figure 9 | The growth curve of HA452 and the upward bias, *r*, of cells over the course of a day. (a) To obtain the growth curve, we sampled cells from the original culture (see "Cell culture" section) at the specified time points (t = 0, 36, 68, 90, 114, 126, 140, 164, 288, 360 h). Cells were counted by imaging them inside the flip chamber, in the middle plane. The growth curve of HA452 in both linear and (Inset) semi-log scale. The population density at carrying capacity was 3×10^5 cells/ml, reached after ~2 weeks of incubation (= 360 h). The population's intrinsic growth rate was found to be 0.4 day^{-1}, as measured by fitting a logistic curve to the data. In the inset, the shaded orange region shows the growth stage at which cells were harvested for experiments with exponential-phase cells (most experiments), while the shaded magenta region denotes the growth stage at which cells were harvested for experiments with starved cells. **(b)** Upward bias, *r*, of HA452 cells over the course of a day, with time measured from midnight. For each data point the equilibrium vertical distribution was measured 30 min after cessation of the overturning treatment, for both 10 flips and 100 flips (for the control: 30 min after introduction of cells in the flipping chamber). A positive upward bias denotes negatively gravitactic cells (*i.e.*, preferentially up-swimming). Gravitaxis can be seen to follow a diel cycle, even though the culture was kept under constant illumination. Flipping experiments consistently show a population' split, by noticing the reduction of the upward bias of the 10 flips and 100 flips treatments compared to the control treatment. The experiments presented in the main text were all conducted between 9 am and 12 noon, where the upward bias measured for the control cells present the maximum stability.

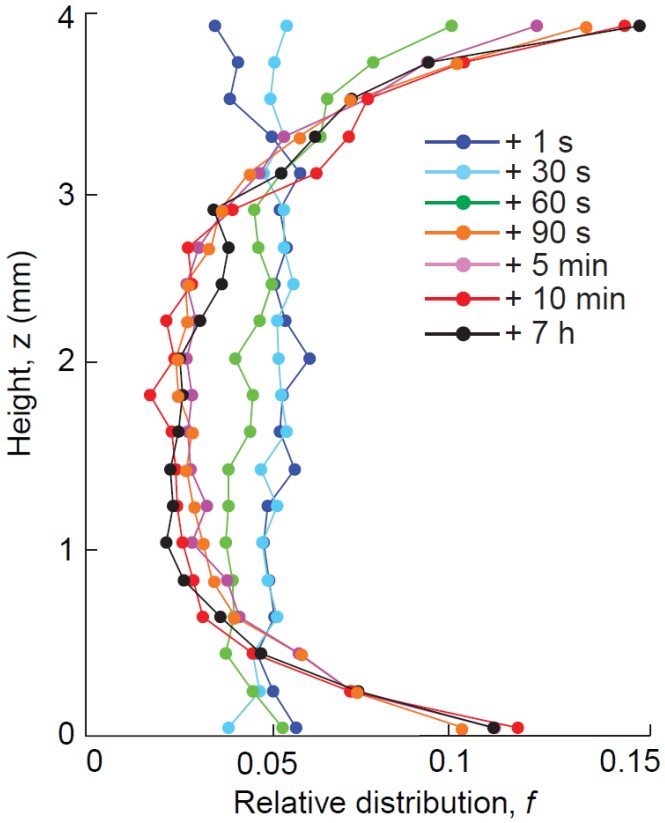

Extended Data Figure 10 | Time series of the vertical distribution of HA452 following a 100-flip treatment. The cell distribution inside the chamber was tracked after the end of the overturning treatment, with time zero corresponding to the cessation of the treatment. At t = 1 s (blue) the cell distribution is homogeneous because the cells have been continuously flipped with a period of 18 s. This timescale is not long enough to allow cells to reach the equilibrium profile, in which the cells reach the top/bottom of the chamber. To traverse the chamber (4 mm) (Extended Data Fig. 2), the time it takes cells swimming with a vertical velocity of 50 µm s^{-1} is 80 s. In fact, it takes 90 s (orange) to establish the bimodal distribution at equilibrium, corresponding to the population split induced by overturning. The population split is then maintained for at least 7 h (black). The upward bias shown in Figs. 1, 2, Extended Data Figs. 1, 8 is always computed 30 min after the overturning ceases.

Supplementary Information

Gravity sensing in HA452. The mechanism by which HA452 perceives its reorientation relative to gravity remains unclear. The large (> 75 µm) unicellular protists *Paramecium* and *Tetrahymena* sense gravity by an active physiological mechanism through mechanosensitive ion-channels[S1,S2] (MSCs, *e.g.*, calcium, potassium), which are activated by to the gravitational pressure of the cytoplasm on the lower membrane. In the flagellate *Euglena gracilis* (35–50 µm), break-down of an existing calcium gradient by means of the ionophore calcimycin (A23187), and gadolinium, as well as manipulating the membrane potential with the lipophilic cation triphenylmethylphosphonium (Ph3MeP +) resulted in a loss of gravitaxis[S3,S4], confirming that changes in the membrane potential are involved in graviperception in that species. For cells in the size range of HA452 (10–15 µm) the work on the lower membrane is of the order of the thermal noise, under the assumption that the whole cytoplasmic material functions as a buoy. Specifically, the work due to the gravitational force on the lower membrane of HA452, assuming 1 nm gating distance of the mechanosensitive ion channels[S1,S5], an average cell length of 15 µm and cell diameter of 10 µm, and a cell density of 1050 kg m^{-3}, is 4×10^{-22} J. The thermal noise at room temperature (293K) is $kT/2 = 2\times10^{-21}$ J, where k is the Boltzmann constant.

The effects of turbulence on motile phytoplankton. There is ample evidence that dinoflagellates and raphidophytes are often negatively impacted by small-scale turbulence, compared for example to diatoms[8], with the main body of literature focusing on dinoflagellates[1]. For instance, a review of the effects of turbulence on phytoplankton[S6] found a negative effect on the growth rates of 70% of the dinoflagellate species assayed.

Negative effects can occur based on at least three mechanisms: physiological impairment, physical damage, and behavioural modification. Turbulence can reduce growth rates and, if sustained, lead to mortality[S7,S8], and large shear rates can induce cellular disintegration[S9]. Turbulence can also negatively affect cells by disrupting various elements of their complex life cycle, such as the cellular clock, mitotic cycle, and nucleic acid concentrations[S8,S9]. It has been hypothesized that the blockage of dinoflagellate division by shaking is caused by physical disturbance of the microtubule assemblage and/or the mechanisms responsible for chromosome separation[S10,S11] and genes involved in cell division, including microtubuli synthesis, are down-regulated upon exposure to turbulence (Elisa Berdalet, pers. comm.). Other negative effects of turbulence include significant (50%) reductions in swimming velocity (*Alexandrium minutum*[S12]), loss of flagella and swimming ability (*Gonyaulax polyedra*[8]), and disruption of vertical migration by trapping[18].

Nitric Oxide (NO) as a stress marker. Nitric oxide (NO) is a highly reactive, free radical that belongs to the family of reactive nitrogen species (RNS) ([S13-S15]). NO accumulation, which under low level mediates cell signalling[S16,S17] and cross-talk with ion-channels[26], in higher level induces cytotoxicity[S18] and cell stress [S13,S19]. Cells produce NO under diverse conditions involving oxidative stress[S13], which suggest a co-regulation of RNS and its

oxidative counterparts – reactive oxygen species (ROS) ([S13]). For instance, nitric oxide synthase produces NO, which is known to react with O_2^- to form the peroxynitrite anion ($ONOO^-$), a potent oxidant[S20]. RNS and ROS can regulate plant and algal responses, both under normal physiological conditions and in response to biotic and abiotic stress (variations in temperature, salinity, pH, light, and physical wounding) through cross-talk between oxidative and nitrosative signalling[26,S21].

In algae and plants, prolonged stress conditions result in nitrosative stress with an overproduction of NO and other RNS ([41,S14,S15]). RNS bursts are commonly observed in marine eukaryotes[S22-S25], including raphidophytes[S26]. While production of low concentrations of NO has been observed in marine phytoplankton under normal growth conditions, variations in the nutrient levels, trace elements, light conditions, temperature, or salinity, can induce changes in the level of NO production[S19,S22-S26]. In particular, significant variations in an environmental stimulus can enhance NO production, potentially as a stress response, as reported for the dinoflagellate *Gymnodinium sp.*[S23] and the raphidophytes *Chattonella marina* and *Heterosigma akashiwo*[S26]. Further examples of enhanced NO production include the response to heat stress of dinoflagellates *Symbiodinium*[S24,S25] and of sponges[S22].

Bet-hedging in HA452. Here we briefly address our interpretation of the observed switch in the direction of migration as a potential bet-hedging strategy. In a strict definition, evolutionary bet-hedging involves a trade-off between the mean fitness and the temporal variance of fitness, such that phenotypes with reduced arithmetic mean fitness may be at a selective advantage under fluctuating environmental conditions[S27]. The diversification of migration strategies observed in HA452 appears to qualitatively meet the two formal requirements of a bet-hedging strategy[S27,S28]: (i) the observed diversification of migration behaviour (Figs. 1,2), together with the initial heterogeneity in orientational stability within a population (Extended Data Fig. 7), will decrease the temporal variance of fitness across multiple generations when the turbulence level fluctuates over time[7]; and (ii) the split of the population will have a cost that reduces fitness, since the downward-swimming subpopulation will give up reaching the well-lit surface waters and thus performing photosynthesis. These considerations support the thesis that the population split observed in HA452 is a bet-hedging strategy, if bet-hedging is interpreted sensu Bulmer[27,S29], where the focus is on the risk-avoidance component of this strategy.

Turbulence is frequently localized within relatively thin layers[7,15,S30]. In view of the often deleterious effect of strong turbulence, the ability to escape these localized regions of high turbulence will provide a benefit to a phytoplankton population. Specifically, as they swim into a layer of high turbulence, cells will experience progressively increasing levels of turbulence (because the turbulent intensity necessarily tapers off below and above the layer): an evasion response would thus prevent the entire population from ending up in the high-turbulence core of the layer and potentially being wiped out. In this context, the behavioural response to moderate levels of turbulence found in our experiments ($\varepsilon = 3\times10^{-8}$ W/kg) can provide a direct benefit to a population. This benefit results from the ability of a fraction of the population to avoid the most damaging turbulence (at the cost of temporarily halting

growth), while a fraction of the population 'attempts the crossing' of the turbulent region (at the risk of suffering damage), a strategy justified by the lack of information on the actual intensity of turbulence and the benefit of reaching shallower depths optimal for photosynthesis.

We highlight, however, that in the interpretation of bet-hedging according to which a population must have lower arithmetic mean fitness and a reduced temporal variance of fitness[S27,S29], we cannot make quantitative conclusions, because in the current setup it is difficult to devise a meaningful definition of fitness appropriate for the environmental conditions that cells face in the ocean for two main reasons:

i) Our observational approach is representative of the time/region when plankton encounter turbulence, and does not capture the dynamics over the entire water column. It is very reasonable to expect that benefits occur in fact at the water column scale, by allowing some cells to attempt swimming through a layer of turbulence and others to seek refuge at depth. Assessing the benefit would thus entail determining the overall growth of the population in the presence of this vertical heterogeneity in turbulence conditions, which demands an entirely different experimental setup, likely one in which turbulent patches or layers lasting for given amounts of time are created.

ii) All experiments were conducted under diffuse room light settings with no vertical gradient, to avoid possible photo-responses[32,37].

For these reasons, we cannot conclusively establish whether this strategy is bet-hedging according to the most stringent definition of the term, yet our evidence corroborates the possibility of this being the case.

References for Supplementary Information

S1. Hemmersbach, R. & Häder, D. P. Graviresponses of certain ciliates and flagellates. *FASEB J.* **13,** S69–S75 (1999).

S2. Richter, P. R., Schuster, M., Wagner, M., Lebert, M. & Häder, D. P. Physiological parameters of gravitaxis in the flagellate *Euglena gracilis* obtained during a parabolic flight campaign. *J. Plant Physiol*. **159**, 181-90 (2002).

S3. Hader, D. P. & Lebert M. Graviperception and gravitaxis in algae. *Adv. Space Res.* **27**, 861–70 (2001).

S4. Richter, P. R., Schuster, M., Lebert, M. & Häder, D. P. Gravitactic signal transduction elements in *Astasia longa* investigated during parabolic flights. *Microgravity Sci. Technol.* **14**, 17-24 (2003).

S5. Philips, R., Kondev J. & Theriot, J. *Physical biology of the cell*. Garland Science, Taylor & Francis Group, LLC, New York (2013).

S6. Berdalet, E. & Estrada, M. Effects of small-scale turbulence on the physiological functioning of marine algae. *Algal Cultures, Analogues and Applications*, New Hampshire, Science Publisher, 459-500 (2005).
S7. White, A. Growth inhibition caused by turbulence in the toxic marine dinoflagellate *Gonyaulax excavata*. *J. Fish. Res. Board Can*. **33**, 2598–2602 (1976).
S8. Pollingher, U. & Zemel, E. In-situ and experimental evidence of the influence of turbulence on cell division processes of *Peridinlum cinctum* forma *westii* (Lemm.). *Lefèvre. Br. Phycol. J.* **16**, 281-287 (1981).
S9. Berdalet, E. & Estrada, M. *Effects of turbulence on several dinoflagellate species. Toxic Phytoplankton Blooms in the Sea*, 734-737, Ed. Smayda, T. J. & Shimizu, Y. (1993).
S10. Karentz, D. Dinoflagellate cell cycles. *Phycotalk*, Ed. Kumar, H. D. Print House Ltd., Maharashtra, India, 377–397 (1987).
S11. Berdalet, E. Effects of turbulence on the marine dinoflagellate *Gymnodinium nelsonii*. *J. Phycol.* **28**, 267–272 (1992).
S12. Chen, D., Muda, K., Jones, K., Leftley, J. & Stansby, P. Effect of shear on growth and motility of *Alexandrium minutum* Halim, a red-tide dinoflagellate. *Harmful Algae. Xunta de Galicia and Intergovernmental Oceanographic Commission of UNESCO, Vigo, Spain*. Ed. Reguera, B., Blanco, J., Fernández, M. L. & Wyatt, T. 352–355 (1998).
S13. Lesser. M. P. Oxidative stress in marine environments: Biochemistry and physiological ecology. *Annu. Rev. Physiol*. **68**, 253-78 (2006).
S14. Arasimowicz. M. & Floryszak-Wieczorek, J. Nitric oxide as a bioactive signalling molecule in plant stress responses. *Plant Science* **172**, 876-887 (2007).
S15. Corpas, F.J., Carreras, A., Valderrama, R. et al. Reactive nitrogen species and nitrosative stress in plants. *Plant Stress* **1**, 37–41 (2007).
S16. Neill, S.J., Desikan, R., Clarke, A., Hurst, R.D. & Hancock, J.T. Hydrogen perxoxide and nitric oxide as signalling molecules in plants. *J. Exp. Bot.* **53**, 1237-1247 (2002).
S17. Vardi, A. *et al.* A stress surveillance system based on calcium and nitric oxide in marine diatoms. *PLoS Biol.* **4,** 411–9 (2006).
S18. Barros. M. P. *et al.* Rhythmicity and oxidative/nitrosative stress in algae. *Biological Rhythm Research* **36**, 67-82 (2005).
S19. Kumar, A., Castellano, I., Patti, F.P., Palumbo, A. & Buia, M.C. Nitric oxide in marine photosynthetic organisms. *Nitric Oxide* **47**, 34-39 (2015).
S20. Halliwell B, Gutteridge JMC. *Free Radicals in Biology and Medicine*. New York: Oxford Univ. Press. 1999.
S21. Molassiotis, A. & Fotopoulos, V. Oxidative and nitrosative signaling in plants: two branches in the same tree? *Plant signaling & behavior* **6**, 210-214 (2011).
S22. Giovine, M. *et al*. Heat stress-activated, calcium-dependent nitric oxide synthase in sponges. *Nitric Oxide* **5,** 427-431 (2001).
S23. Zhang, Z. B. *et al*. Detection of nitric oxide in culture media and studies on nitric oxide formation by marine microalgae. *Medical science monitor* **12**, BR75-BR85 (2006).
S24. Bouchard, J.N. & Yamasaki, H. Heat stress stimulates nitric oxide production in *Symbiodinium microadriaticum*: a possible linkage between nitric oxide and the coral bleaching phenomenon. *Plant Cell Physiol*. **49**, 641-52 (2008).
S25. Hawkins, T. D. & Davy, S. K. Nitric oxide production and tolerance differ among *Symbiodinium* types exposed to heat stress. *Plant and Cell Physiology* **53**, 1889-1898 (2012).

S26. Kim, D. et al. Detection of Nitric Oxide (NO) in Marine Phytoplankters. *J. Biosci. Bioeng.* **105**, 414-7 (2008).
S27. Philippi, T. & Seger, J. Hedging one's evolutionary bets, revisited. *Trends Ecol. Evol.* **4**, 2–5 (1989).
S28. Seger, J. & Brockmann, H. J. What is bet-hedging? *Oxford surveys in evolutionary biology* **4**, 182-211. Oxford University Press (1987).
S29. Ripa, J., Olofsson, H. & Jonzen, N. What is bet-hedging, really? *Proc. R. Soc. B.* **277**, 1153-4 (2010).
S30. Doubell, M. J., Prairie, J. C. & Yamazaki, H. Millimeter scale profiles of chlorophyll fluorescence: Deciphering the microscale spatial structure of phytoplankton. *Deep. Res.* (2014).